12-2009

Analysis of GaN/AlxGa1?xN Heterojunction Dual-Band Photodetectors Using Capacitance Profiling Techniques

Laura E. Byrum
Georgia State University

ANALYSIS OF GaN/$Al_xGa_{1-x}N$ HETEROJUNCTION DUAL-BAND PHOTODETECTORS USING CAPACITANCE PROFILING TECHNIQUES

by

LAURA E. BYRUM

Under the direction of Unil Perera

ABSTRACT

Capacitance-voltage-frequency measurements on n^+-GaN/$Al_xGa_{1-x}N$ UV/IR dual-band detectors are reported. The presence of shallow Si-donor, deep Si-donor, and C-donor/N-vacancy defect states were found to significantly alter the electrical characteristics of the detectors. The barrier Al fraction was found to change the position of the interface defect states relative to the Fermi level. The sample with Al fraction of 0.1 shows a distinct capacitance-step and hysteresis, which is attributed to C-donor/N-vacancy electron trap states located above the Fermi level (200 meV) at the heterointerface; whereas, the sample with Al fraction of 0.026 shows negative capacitance and dispersion, indicating C-donor/N-vacancy and deep Si-donor defect states located below the Fermi level (88 meV). When an i-GaN buffer layer was added to the structure, an anomalous high-frequency capacitance peak was observed and attributed to resonance scattering due to hybridization of localized Si-donor states in the band gap with conduction band states at the i-GaN/n^+-GaN interface.

INDEX WORDS: Infrared detectors, Dual-band, Ultraviolet detectors, III-V material, GaN, AlGaN, Heterojunction, Workfunction, Photoemission, Impurity states, Capacitance, Negative capacitance, Capacitance hysteresis

ANALYSIS OF GaN/$Al_xGa_{1-x}N$ HETEROJUNCTION DUAL-BAND PHOTODETECTORS USING CAPACITANCE PROFILING TECHNIQUES

by

LAURA E. BYRUM

A Thesis Submitted in Partial Fulfillment of the Requirements for the Degree of

Master of Science

in the College of Arts and Sciences

Georgia State University

2009

ANALYSIS OF GaN/$Al_xGa_{1-x}N$ HETEROJUNCTION DUAL-BAND PHOTODETECTORS USING CAPACITANCE PROFILING TECHNIQUES

by

LAURA E. BYRUM

Committee Chair:	Dr. Unil Perera
Committee:	Dr. Nikolaus Dietz
	Dr. Xiaochun He

Electronic Version Approved:

Office of Graduate Studies
College of Arts and Sciences
Georgia State University
December 2009

To my grandparents Bernard and Selma Kessler.

Acknowledgments

I would like to acknowledge my advisor Dr Perera for allowing me to work in his research group and for all the guidance along the way. I learned a tremendous amount about the research process and other invaluable skills. I would also like to thank my other committee members Dr Dietz and Dr He for their insights and suggestions. Finally, I would like to thank all my family and friends for their infinite patience and support.

Table of Contents

List of Tables

List of Figures

Acronyms

Al	aluminum
BC	bottom-contact
C_0	geometric capacitance
C	carbon
CB	conduction band
C-f	capacitance-frequency
C-f-T	capacitance-frequency-temperature
C-V	capacitance-voltage
C-V-T	capacitance-voltage-temperature
Δ	workfunction
Δ_d	band gap offset from doping
Δ_x	band gap offset from barrier Al fraction
e	electron charge
E_C	conduction band energy
E_F	Fermi energy
E_V	valence band energy
f^{-1}	inverse relaxation time
FIR	far-infrared (30-100 μm)
FTIR	Fourier Transform Infrared
FDCD	frequency-dependent capacitance dispersion
Ga	gallium

HEIWIP	Heterojunction Interfacial Workfunction Internal Photoemission
IB	impurity band
IR	infrared
k_F	Fermi momentum
λ_0	zero response threshold
$m^\star$	effective electron mass
MC	middle-contact
MIR	mid-infrared (5-30 μm)
MOCVD	Metal-Organic Chemical Vapor Deposition
N	nitrogen
n	free carrier concentration
n_D	doping concentration
n_{MT}	Mott transition concentration
NIR	near-infrared (0.8-5 μm)
Si	silicon
τ	electron relaxation time
TC	top-contact
UV	ultraviolet
VB	valence band
x	barrier Al concentration

Chapter 1

Introduction

Dual-band GaAs and Si based photodetectors operating in the near- and mid/far-infrared (IR) ranges have been previously reported. [1,2,3] Using GaN/AlGaN based materials, dual-band detection was extended to operate in both the ultraviolet (UV) and infrared (IR) ranges. [4] The wide band gap of GaN enables the fabrication of unique UV/IR dual-band detectors, suited for a wide range of applications such as space situational awareness, flame detection, military sensing, and industrial applications. [5] Such detectors are radiation-hard, solar blind, and relatively resistant to thermal carrier emission and interband tunneling. [6,7] High-quality GaN based device structures are presently limited by the presence of defect states at interface junctions, induced either by lattice mismatch, interface roughness, or interfacial bonding mismatch. [8]

Using capacitance-voltage (C-V) and capacitance-frequency (C-f) measurements the effects of defect induced trap states on the electrical behavior of the dual-band detectors were studied. While this profiling technique reveals the location and mechanisms by which the defect states operate, other methods of analysis are needed to identify the sources of the defect states.

This thesis is organized as follows. **Chapter one** provides a detailed description of the UV/IR dual-band detection mechanism in n^+-GaN/$Al_xGa_{1-x}N$ Heterojunction Interfacial Work-

function Internal Photoemission (HEIWIP) detectors. A discussion of Si doping in GaN materials is provided, in addition to an explanation of the theory behind the capacitance-voltage-frequency (C-V-f) profiling techniques.

Chapter two presents experimental C-V-f results for the 2-contact UV/IR dual-band detectors (samples 1547 and 1158). The mechanisms responsibly for the observed frequency-dependent capacitance dispersion (FDCD), capacitance-step, and capacitance hysteresis in sample 1547 and negative capacitance in sample 1158 is analyzed. The effects of Al fraction on trap state energies (relative to the Fermi level), and subsequent capacitance characteristics are also discussed.

Chapter three includes a discussion of C-V-f characteristics of more complex 3-contact UV/IR dual-band HEIWIP detectors (samples 1291 and 1300). The effects of resonance scattering and hybridization on the capacitance-frequency profiles for a n^+-GaN/$Al_xGa_{1-x}N$ structure are reported. In addition, complex relaxation time is discussed.

1.1 HEIWIP Detection Mechanisms

Nitride-based dual-band Heterojunction Interfacial Workfunction Internal Photoemission (HEIWIP) detectors are capable of detecting both UV and IR radiation. The IR detection is based on the intraband transition from the n^+-GaN emitter, [7] while UV detection is based on interband transitions in the AlGaN barrier. [4]

The detector responds to IR radiation through a three stage process: free carrier absorption, internal photoemission, and (under an external electric field) collection of emitted carriers at the contact. A schematic of the detection mechanism is depicted in Fig. 1.1.

The use of different band-gap materials for the emitter and barrier layers in the detector introduces a workfunction Δ (in meV) defined as the offset between the Fermi level in the n^+-GaN

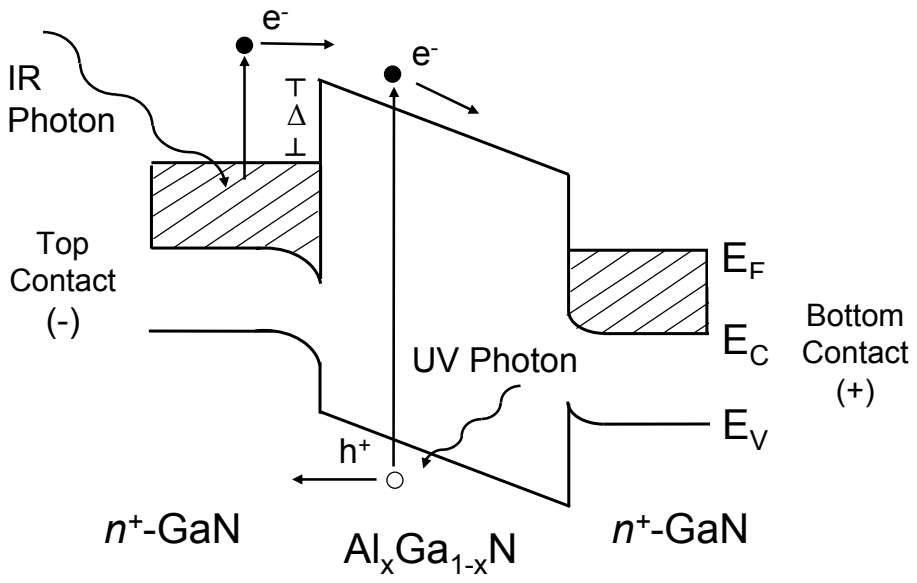

Figure 1.1: The dual-band detector operates by collecting carriers from intraband IR transitions in the n^+-GaN emitter layer and interband UV transitions in the $Al_xGa_{1-x}N$ barrier layer. The work function Δ was 88 meV for the 1158 series and 200 meV for the 1547 series.

emitter layer and the conduction band in the $Al_xGa_{1-x}N$ barrier. The Fermi energy E_F is:

$$E_F = \frac{\hbar^2 {k_F}^2}{2m^\star} \tag{1.1}$$

where $m^\star$ is the effective electron mass and k_F is the Fermi momentum:

$${k_F}^2 = (3\pi^2 n)^{2/3} \tag{1.2}$$

n is the free carrier concentration. This workfunction determines the IR threshold wavelength λ_0 (in μm), as IR response is only possible if the photoexcited carries are able to surmount the barrier.

$$\lambda_0 = 1240/\Delta \tag{1.3}$$

In a heterostructure, the workfunction is determined by the band gap offsets from both doping Δ_d and Al fraction Δ_x:

$$\Delta = \Delta_d + \Delta_x. \tag{1.4}$$

Due to the high doping concentration in the contact layers, the Fermi level lies above the conduction band minimum. Thus, the n^+-GaN/$Al_xGa_{1-x}N$ interface is analogous to a metal-semiconductor interface, as the doping concentration n_D exceeds the metal-insulator (Mott) transition concentration n_{MT} in n^+-GaN.

Dual-band near- and mid/far-IR detectors also have been developed. [3] In a GaAs Homojunction Interfacial Workfunction Internal Photoemission (HIWIP) detectors, the p-GaAs/i-GaAs homojunction introduces a workfunction that is dependent only on the band gap offset from differences in doping between the emitter and barrier layers.

UV light detection takes place in the $Al_xGa_{1-x}N$ barrier layer when an absorbed photon generates an electron-hole pair through the interband transition of the photoexcited electron from the valence band to the conduction band. Assisted by an external electric field, the carriers will be transported out of the UV-active barrier region and collected at the contacts. The UV threshold wavelength λ_{0G} (in nm) is dependent on the band gap of the barrier, given by

$$\lambda_{0G} = 1240/E_G \tag{1.5}$$

where E_G is the band gap between the valence and conduction bands. [9] In $Al_xGa_{1-x}N$, the band gap at room temperature is given by [9]

$$E_G = 6.13x + 3.42(1-x) - 1.08x(1-x). \tag{1.6}$$

Variations in the barrier layer Al content x, as well as the contact layer doping concentration will change the UV and IR threshold. At present, however, the increased Al content has been found [8] to contribute to a significant number of interfacial defect states that limits the detector performance.

A Perkin Elmer System 2000 Fourier transfor infrared spectrometer (FTIR) was used for IR spectral measurements. UV spectral measurements were obtained using an Oriel Deuterium UV

source, UV/VIS monochrometer, and neutral density filters. A schematic of the IR and UV setups are shown in Fig. 1.2(a) and (b). For simultaneous UV/IR detection, the setup shown in Fig. 1.3 was used. The dual-band spectra from a n^+-GaN/$Al_{0.1}Ga_{0.9}N$ and n^+-GaN/$Al_{0.026}Ga_{0.974}N$ HEIWIP detectors are shown in Fig. 1.4(a) and (b), respectively.

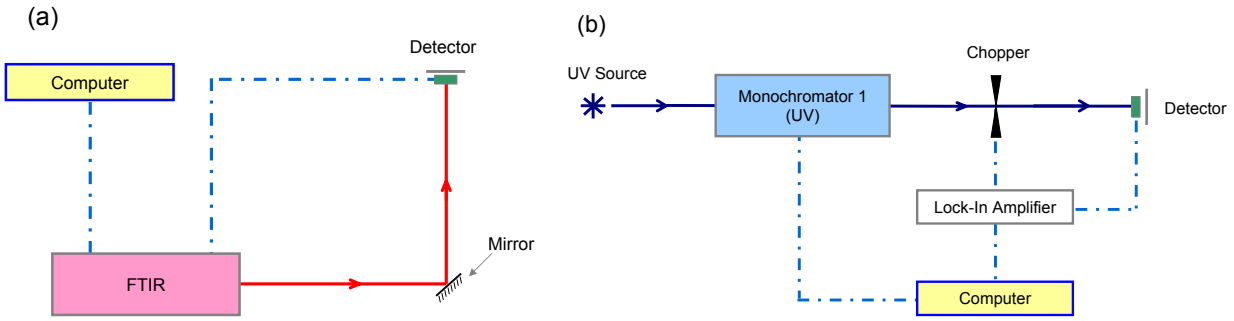

Figure 1.2: Schematic of the setups used to separately measure (a) IR and (b) UV spectral response.

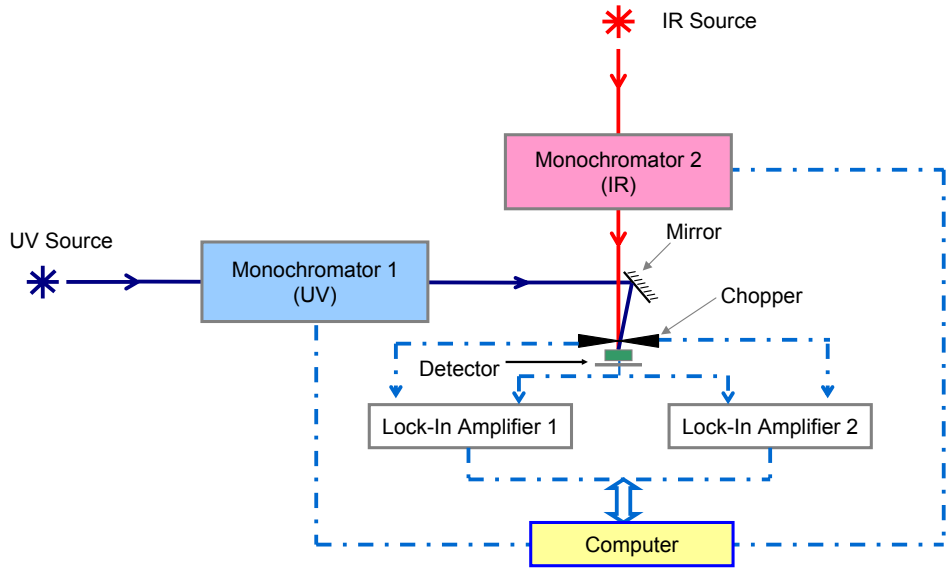

Figure 1.3: Setup used for simultaneous UV/IR spectral response measurements.

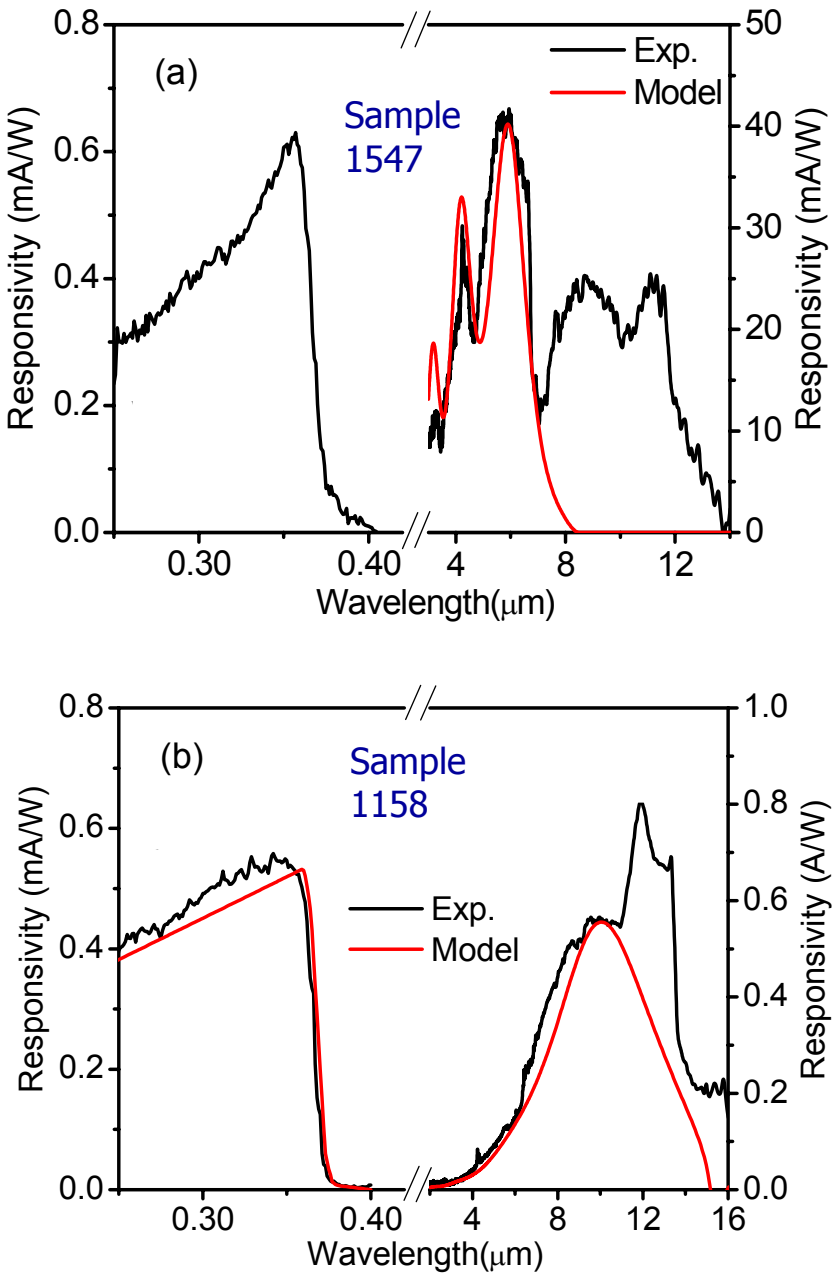

Figure 1.4: Dual-band UV/IR response from the (a) 1547 and (b) 1158 photodetectors. The red line indicates the theoretical responsivity for the detector structures with Al fractions of 0.1 and 0.026, respectively. Deviations from the theoretical responsivity are thought to result from defect related absorption centers.

1.2 Doping in III-V Semiconductors

Silicon is a common shallow donor impurity used to n-dope GaN. At doping densities far below the Mott concentration ($n_D \ll n_{MT}$), the impurities have well defined, discrete ground state energy levels. These localized states are located below the conduction band minimum in the band gap and there is very little interaction between adjacent impurities. As the impurity concentration increases ($n_D < n_{MT}$), adjacent impurities begin to interact, leading to delocalized wavefunctions. The energy levels are no longer localized, but rather form an impurity band. The impurity band will continue to widen as the impurity concentration is increased, until it eventually merges with the conduction band minimum ($n_D \simeq n_{MT}$). At the Mott-transition concentration, the system will transition to a metallic-like state.[10,11,12] In Si-doped GaN, the Mott-transition concentration is 8×10^{17} cm^{-3}. [13] A schematic of the energy transitions with increasing doping concentration is depicted in Fig. 1.5.

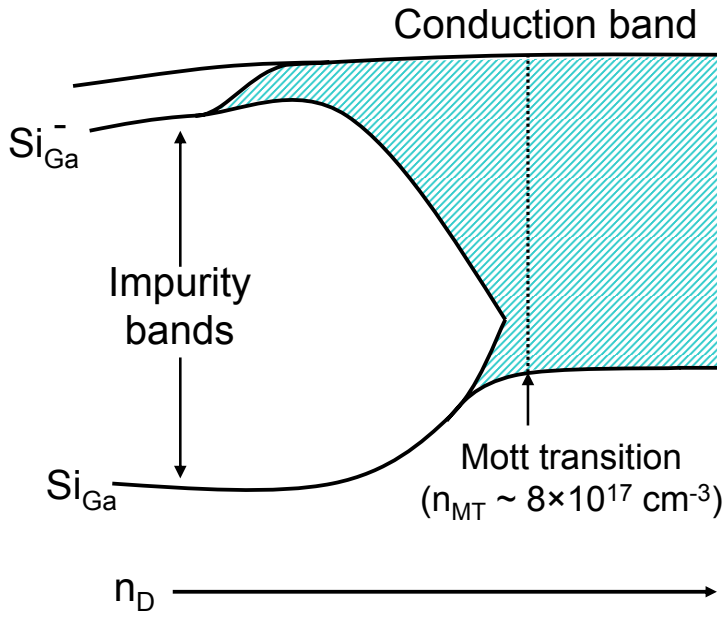

Figure 1.5: Doping profile showing the transition from localized energy states to impurity bands as the doping concentration is increased. At the Mott transition n_{MT}, the impurity band and conduction band merge. Figure modified from Ref. [11].

1.3 Use of Capacitance Measurements as a Profiling Technique

Capacitance measurements allow the determination of charge distribution and the identification of the presence of interface states in semiconductors, as an applied bias contributes to carrier capture and emission at interface trap states. These trap states will become charged and, thus, produce a dipole layer in the vicinity of the heterojunction.[7] Small modulations in ac bias will cause a change in the barrier height, and the position of the Fermi level will shift relative to its equilibrium position, thus, changing the characteristics of the detector.

Different aspects of the electrical behavior can be studied using C-V and C-f characteristics. For C-f measurements, the applied dc voltage is held constant and the ac frequency varied; whereas, for C-V measurements, the ac frequency is held constant and the applied dc voltage is varied. The computer-controlled Hewlett Packard 4284A LCR meter setup is depicted in Fig. 1.6.

If the frequency of the ac signal exceeds the inverse relaxation times of the trap states, the states cannot follow the ac signal due to finite inertia. The capacitance profile will then reflect the geometric capacitance of the sample, as if no trap states were present. As the ac frequency is decreased, trap states will be able to respond, but lag behind, the ac signal. [10] For trap states with inverse relaxation times faster than the ac bias, the trap states will be able to follow the ac signal and variations in capacitance will be observed.

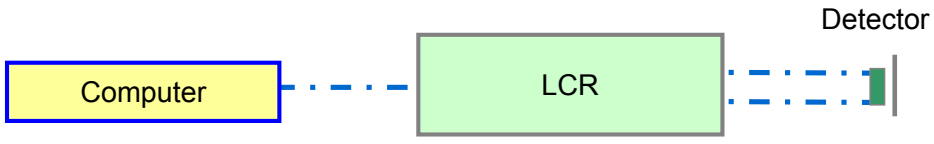

Figure 1.6: The computer-controlled Hewlett Packard 4284A LCR meter setup used to take C-V-f measurements of the dual-band detector structures.

Chapter 2

n^+-GaN/$Al_xGa_{1-x}N$/n^+-GaN Dual-band Detectors (2-contact)

Capacitance-voltage-frequency measurements on n^+-GaN/$Al_xGa_{1-x}N$ Heterojunction Interfacial Workfunction Internal Photoemission (HEIWIP) detectors were used to analyze the effects of Al fraction induced heterojunction barrier and its effect on the electrical characteristics at the heterointerface. A sample with an Al fraction of 0.1 (sample 1547) shows a distinct capacitance step and capacitance hysteresis, which is attributed to C-donor and/or N-vacancy electron trap states located just above the Fermi level (200 meV) at the GaN/AlGaN interface, with activation energies of 149±1 and ∼189 meV, respectively. A sample with an Al fraction of 0.026 (sample 1158) showed negative capacitance and dispersion, indicating interface electron trap states located below the Fermi level (88 meV), most likely due to C-donor/N-vacancy and deep Si-donor states with activation energies of 125±1 and 140±2 meV, respectively. Additional impurity related absorption centers were identified in both samples, however these shallow Si-donor sites (∼30.9±0.2 meV) did not affect the capacitance as these states were located in the barrier layer and not in the vicinity of the Fermi level. The Al fraction in the barrier layer was found to significantly change the posi-

tions of the interface trap states relative to the Fermi level, resulting in the observed capacitance characteristics.

2.1 Device Growth and Processing

The 2-contact n^+-GaN/$Al_xGa_{1-x}N$/n^+-GaN dual-band UV/IR detectors were grown by low pressure Metal-Organic Chemical Vapor Deposition (MOCVD) on a *c*-plane sapphire substrate. As depicted in Fig. 2.1 (a), the 2-contact structures consist of a 0.2 μm n^+-doped GaN top-contact (TC) emitter layer, a 0.6 μm $Al_xGa_{1-x}N$ barrier layer, and a 0.7 μm n^+-doped GaN bottom-contact (BC) layer. The $Al_xGa_{1-x}N$ barrier layers in the 1547 and 1158 samples have Al fractions of 0.1 and 0.026, respectively. The TC and BC layers in both samples are n^+-doped with silicon to a doping concentration of 5×10^{18} cm^{-3}.

Dry etching techniques were used to form square mesas on all samples, and in some cases reduce or remove the IR-active TC layer. Etching the TC emitter will drastically reduce the IR-active region of the sample. Ohmic Ti/Al/Ti/Au contacts were deposited onto the n^+-GaN TC and BC layers. The structures were then annealed for 2 min under nitrogen gas flow at 700°C. A schematic of the rectangular contact is depicted in Fig. 2.1 (b).

When etching, only the areas between the metal contacts were removed. The n^+-GaN layer under the metal rectangular contacts remained unetched (0.2 μm thick). Thus, even in the fully-etched sample, n^+-GaN is still present between the metal contacts and the $Al_xGa_{1-x}N$ barrier, as the n^+-GaN layer must remain between the metal contact and the $Al_xGa_{1-x}N$ barrier for carriers to be collected.

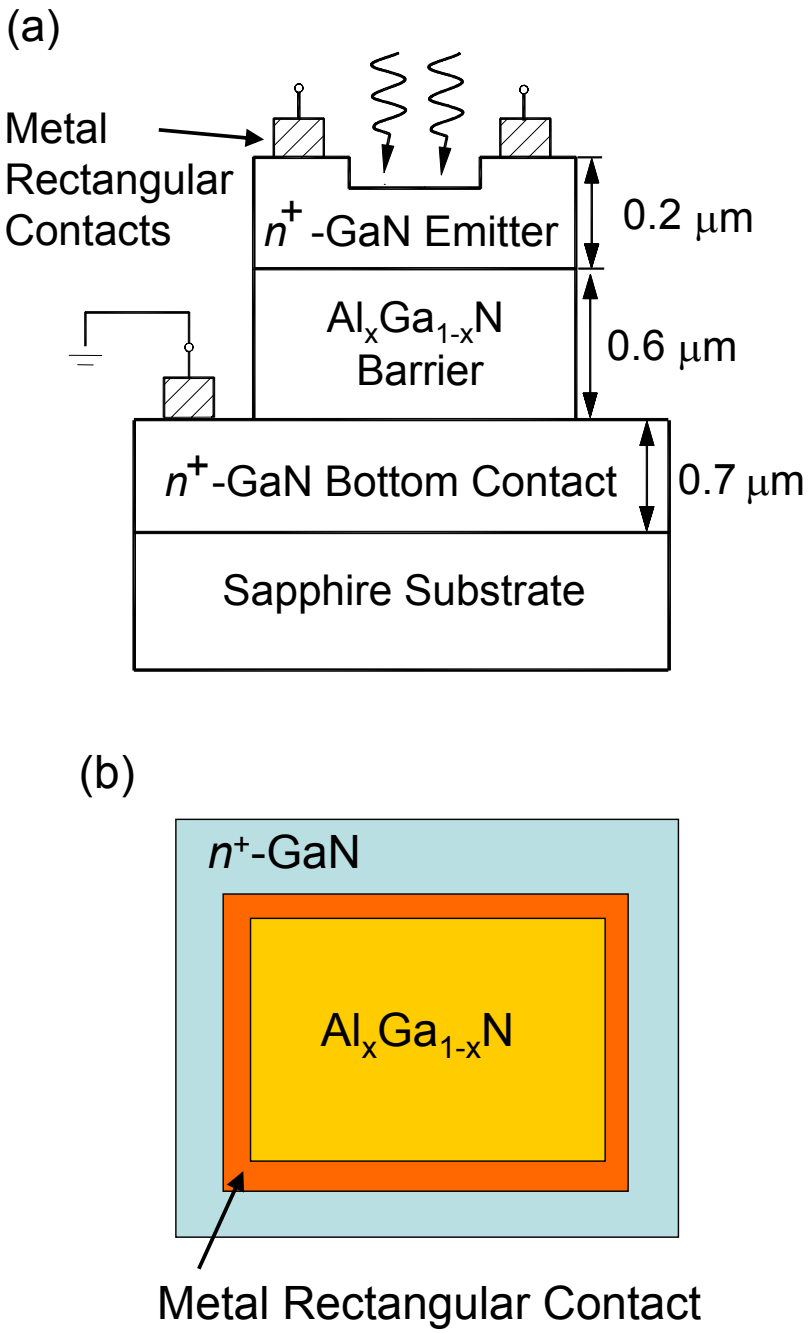

Figure 2.1: (a) The 2-contact structures consist of an undoped $Al_xGa_{1-x}N$ barrier layer between n^+-GaN TC and BC layers. The 1547 and 1158 samples have Al fractions of 0.1 and 0.026, respectively. When the sample is reverse biased, the TC layer will act as an emitter. Both n^+-GaN layers are doped with Si to a concentration of 5×10^{18} cm^{-3}. (b) Top view of the structure showing the metal rectangular contact.

2.2 Sample 1547: 0.1 Al fraction

The response peak observed in the IR spectra (see Fig. 2.2) between 3 and 8 μm is due to free carrier absorption. IR spectroscopy revealed impurity related absorption centers with transitional energies of 23.2±0.1, 112±0.5 and ∼142 meV, correspond to activation energies of 30.9±0.1 149±1 and ∼189 meV, respectively. The defect energy state with an activation energy of 30.9±0.1 meV was attributed to shallow Si-donor imputities in the $Al_{0.1}Ga_{0.9}N$ barrier layer. C-donor/N-vacancy defects at the heterointerface with states above the Fermi level are thought to account for the states with activation energies of 149±1 meV. The origin of the defect states associated with an activation energy of ∼189 meV is still unknown, but could possibly be due to deep Si-donor impurities at the heterojunction.

Capacitance-voltage (C-V) and capacitance-frequency (C-f) measurements were carried out using a computer-controlled Hewlett Packard 4284A LCR meter. Capacitance scans were run between -2 V and +2 V with the TC biased and the BC grounded at frequencies ranging from 100 Hz to 1 MHz. When forward biased, the TC is positive and the BC is negative. Under reverse bias the TC is negative and the BC is positive.

2.2.1 Capacitance Hysteresis

Capacitance-steps in the C-V profiles of sample 1547, shown in Fig. 2.3(a), are believed to result from an abrupt change in carrier trap occupation due to C-donor and/or N-vacancy defect energy states located slightly above the Fermi level at the n^+-GaN/$Al_{0.1}Ga_{0.9}N$ interface. These defect states most likely have an energy band associated with them, as opposed to a discrete energy state. As shown in the band diagrams of sample 1547 at zero bias, Fig. 2.4(a), defect states above the Fermi level are empty; but when the bias reaches a critical value, shown in Fig. 2.4(b), the

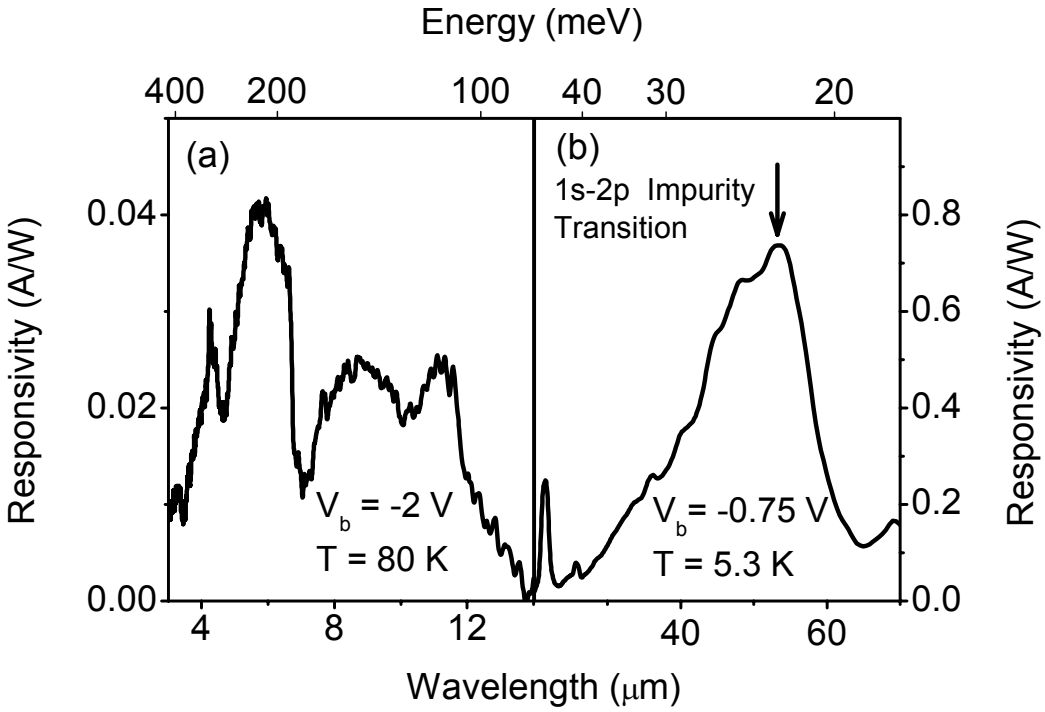

Figure 2.2: (a) IR spectra of sample 1547 showing two impurity related absorption centers with transitional energies of 112±0.5 and ∼142 meV, corresponding to activation energies of 149±1 and ∼189 meV. These absorption centers were attributed to C-donor/N-vacancy and an unkown defect state, respectively. (b) A third absorption center was observed in the IR spectra with a 1s-2p± transitional energy of 23.2±0.1 meV. This absorption center was attributed to shallow Si-donor states in the $Al_{0.1}Ga_{0.9}N$ barrier layer with an activation energy of 30.9±0.2 meV.

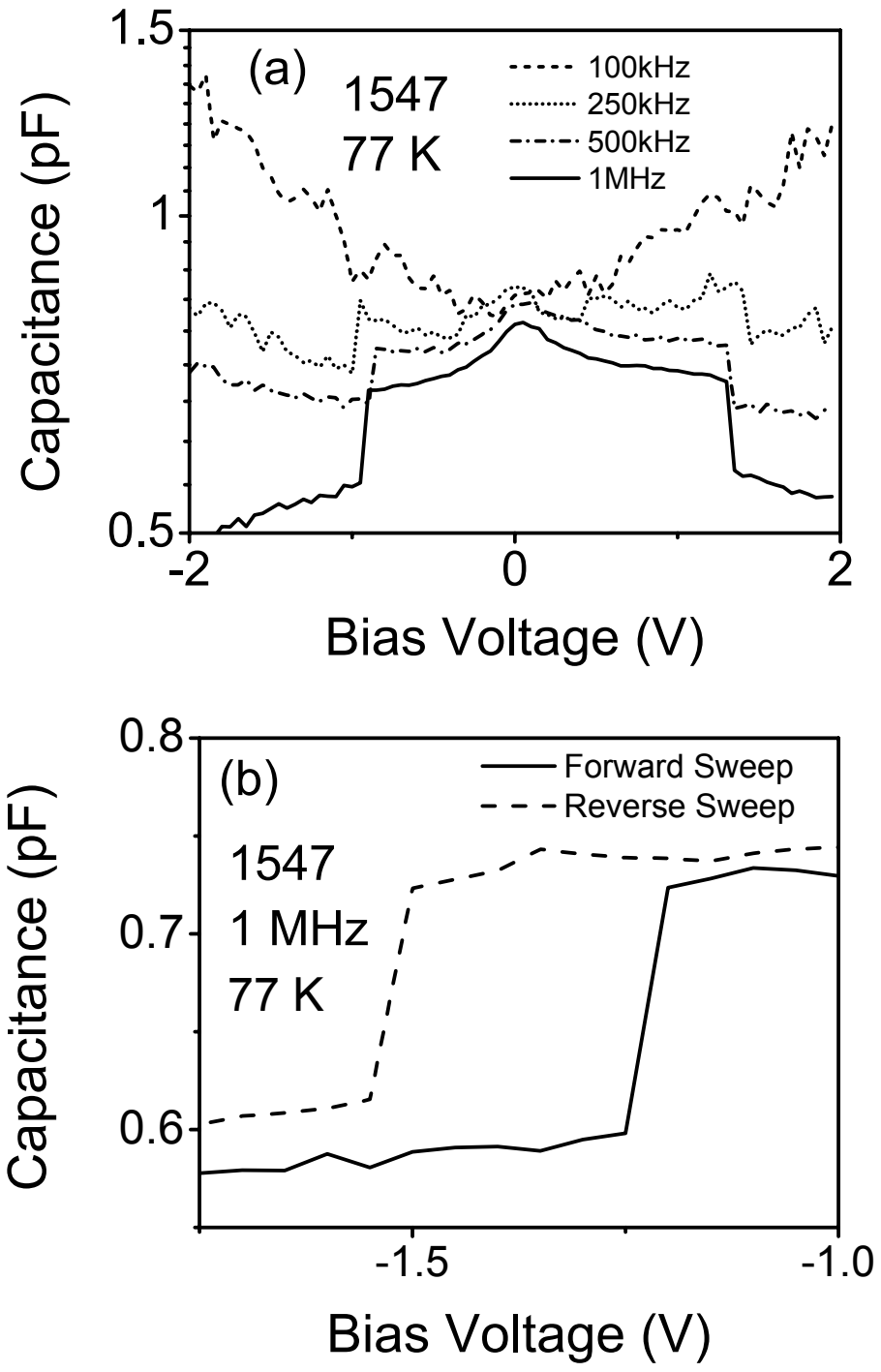

Figure 2.3: C-V profiles of sample 1547 showing (a) frequency-dependent capacitance dispersion and a capacitance-step. The capacitance-step became more pronounced as frequency increased. (b) The capacitance hysteresis between forward and reverse scans. The vertical offset is within the noise range.

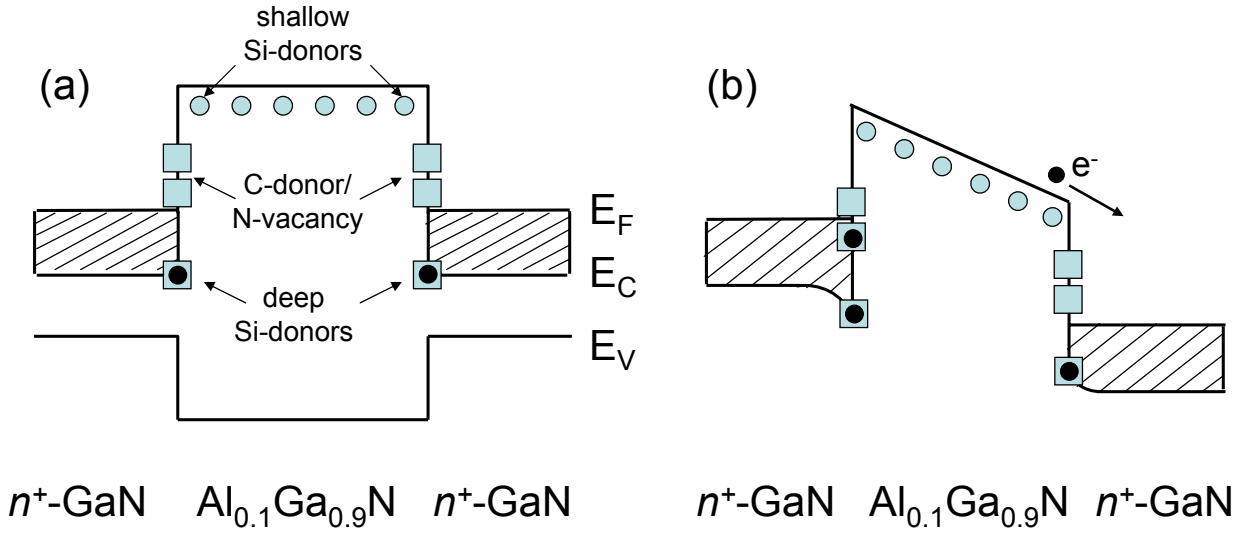

Figure 2.4: Band diagram for sample 1547 at (a) zero bias and (b) reverse bias. At zero bias the C-donor and N-vacancy defect states were located above the Fermi level. As the bias became more negative, the Fermi level swept through the interface trap states, causing the abrupt increase/decrease in capacitance. In the figure, the n^+-GaN TC is to the left of the intrinsic $Al_{0.1}Ga_{0.9}N$ barrier layer and the n^+-GaN BC is to the right; the diagram is intended to show the area between metal contacts.

Fermi level enters the previously unoccupied defect state bands. Thus, carriers can readily move in and out of the defect states, leading to an increase in capacitance. Conversely, when the Fermi level sweeps out of the occupied defect state bands, the capacitance suddenly decreases as the defect states can no longer contribute to capacitance.

Simulated results [14] indicate that relaxation time constants for generation and recombination processes at defect related states are dependent on carrier concentration. The electron recombination (capture) relaxation time τ_r and the electron generation (emission) relaxation time τ_g are

$$\tau_r = (\sigma_n v_{th} n)^{-1} \tag{2.1}$$

and

$$\tau_g = (\sigma_n v_{th} n_1)^{-1} \tag{2.2}$$

where σ_n is the capture cross section and v_{th} is the thermal velocity. n is the non-equalibrium concentration of mobile electrons

$$n = n_i \exp\left(\frac{e[\phi_{F_n} - \phi]}{k_B T}\right) \tag{2.3}$$

and n_i is the intrinsic density.

$$n_1 = N_C \exp\left(\frac{[E_C - E_t]}{k_B T}\right) \tag{2.4}$$

where e and $k_B T$ denote the electron charge and thermal energy at specific temperature, respectively. Both expressions are of similar form, however, the non-equilibrium concentration n depends on the intrinsic density and the quasi-Fermi potential of the electrons ϕ_{F_n} and the electrical potential of the work function ϕ; whereas n_1 depends on the effective electron density of states N_C and the position of the trap state energy E_t relative to the conduction band edge E_C. Thus, n_1 and τ_g are not susceptible to bias induced band bending. [14]

The hysteresis in the C-V profile for sample 1547, shown in Fig. 2.3(b), can be explained as follows. With a forward scan direction, the C-donor/N-vacancy defect states are initially empty. These energy states act as acceptor-like electron trap states. As the bias increases, the Fermi level will move through the trap states, thus, filling the trap states and causing an abrupt change in carrier concentration. As these trap states become occupied, negative charges will build up at the interface, resulting in an accumulation region. When the scan direction is reversed, the C-donor/N-vacancy defect states are initially filled. The residual charge in the accumulation region leads to lower effective fields at the interface and, hence, a higher required voltage for the capacitance-step, which occurs as the Fermi level moves out of the energy continuum and the trap states are abruptly emptied. The difference in initial carrier occupation of the C-donor/N-vacancy defect states between a forward and reverse scan direction results in the observed hysteresis.

At low carrier concentrations the trap state relaxation times are still fast enough to respond

to the applied ac bias, so although an abrupt capacitance-step will occur, the trap states can emit carriers fast enough to prevent a significant buildup of charges at the interface. At sufficiently high carrier concentrations, the relaxation times of the energy states decreases to a point where the charging process can no longer follow the voltage modulation. Since carriers captured in the trap states cannot be emitted fast enough, a residual charge will remain at the interface when the scan direction is reversed, resulting in the capacitance hysteresis.

The presence of interface frequency-dependent trap states was responsible for the observed capacitance dispersion in the C-V profiles. Frequency-dependent capacitance dispersion (FDCD) has been observed [8,16] in other GaN/AlGaN heterojunction structures in the 10 kHz to 1 MHz regions with corresponding relaxation time constants of 1 and 63 μs, respectively. In sample 1547, trap state relaxation times could be calculated from the C-f profile, and ranged from 68-107 μs at 77 K. A single relaxation time cannot be identified [14] because relaxation times are dependent on carrier concentration (see eqn. 2.1), rather a broad range of relaxation times is observed.

2.3 Sample 1158: 0.026 Al fraction

The broad response peak observed in the IR spectra (see Fig. 2.5) between 8 and 14 μm is due to free carrier absorption. However, absorption peaks related to impurity transitions are observed superimposed on the free carrier response between 11 and 13.6 μm. Based on previous reports, [20,21] the three impurity related absorption peaks were attributed to shallow Si-donor impurities in the $Al_{0.0.26}Ga_{0.974}N$ barrier layer with a 1s-2p$\pm$ transitional energy of 23.1$\pm$0.1 meV, which corresponds to an activation energy of 30.8$\pm$0.2 meV. C-donor/N-vacancy defect states were attributed [22,23] to the transitional energy of approximately 93.4$\pm$0.5 meV, which correspond to an activation energy of 125$\pm$1 meV. The third peak with a transitional energy of 105$\pm$1.5 meV and

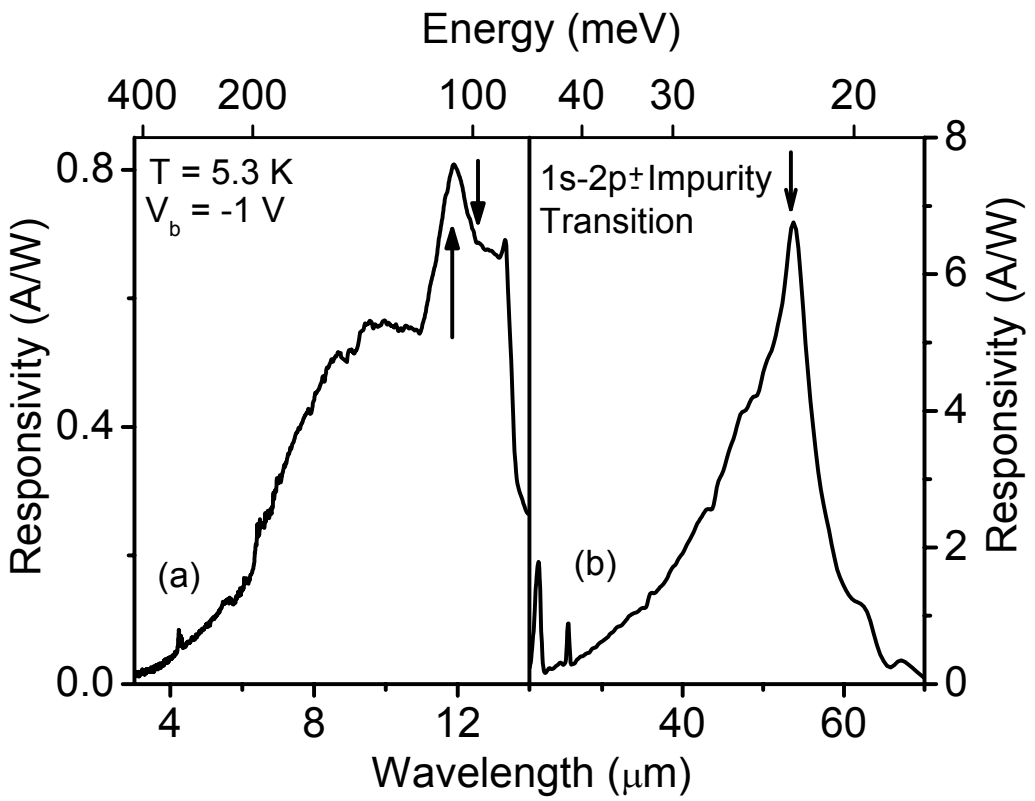

Figure 2.5: (a) IR spectra of sample 1158 showing two impurity related absorption centers with transitional energies of 93.4±0.5 and 105±1.5 meV, corresponding to activation energies of 125±1 and 140±2 meV. These absorption centers were attributed to C-donor/N-vacancy and deep Si-donor defect states, respectively. (b) A third absorption center was observed in the IR spectra with a 1s-2p± transitional energy of 23.1±0.1 meV. This absorption center was attributed to shallow Si-donor states in the $Al_{0.026}Ga_{0.974}N$ barrier layer with an activation energy of 30.8±0.2 meV.

activation energy of 140±2 meV is attributed to Si-donor states at the n^+-GaN/$Al_{0.0.26}Ga_{0.974}N$ heterointerface, that are pinned to the impurity band in the n^+-GaN emitter layer. The conduction band offset of the n^+-GaN/$Al_{0.0.26}Ga_{0.974}N$ heterointerface was calculated to be 137±7 meV, which is consistent with the activation energy of 140±2 meV.

C-V and C-f measurements were carried out using a computer-controlled Hewlett-Packard 4284A LCR meter. C-V scans were taken from -2 V to +2 V with a 50 mV step width and sine output amplitude set at 5 mV from 100 Hz - 1 MHz, while the C-f scans were taken between 1 kHz and 1 MHz. When forward biased, the TC is positive and the BC is negative. Under reverse bias

the TC is negative and the BC is positive. In the C-V profiles (see Fig. 2.6), negative capacitance was observed at frequencies of 10 - 500 kHz, which falls in the range of ∼6 - 600 kHz where negative capacitance occurred in the C-f profiles.

2.3.1 Negative Capacitance

When described in terms of charge accumulation at an interface, capacitance is defined in terms of electrostatics:

$$C_0 = \frac{\epsilon\epsilon_0 A}{L} \tag{2.5}$$

where ϵ is the relative dielectric permittivity, ϵ_0 is the dielectric permittivity in a vacuum, A is the mesa area, and L is the thickness of the barrier layer. However, this description can only result in positive capacitance as the total electric current is due solely to the displacement current and there is no contribution from a conduction current. Only in specific cases (high frequency or low temperature) can the capacitance be described by the electrostatic approximation, referred to as the geometric capacitance C_0. The geometric capacitance for sample 1158 with 600μm × 600μm mesa area is ∼2.9 pF.

In order to describe negative capacitance in terms of transient currents [17] (in the time domain) and capacitance (in the frequency domain), capacitance must be defined in terms of the reactive part of the total current (both the conduction and displacement currents):

$$C(\omega) = \frac{1}{\omega} Im[Y(\omega)] = \frac{1}{\Delta V} \int_0^\infty \delta J(t) \cos(\omega t) dt. \tag{2.6}$$

When the transient current $J(t)$, transient relaxation current $\delta j(t)$, and geometric capacitance C_0 are included, the capacitance is described [17] by:

$$C(\omega) = C_0 + \frac{1}{\omega \Delta V} \int_0^\infty \frac{-d\delta j(t)}{dt} \sin(\omega t) dt. \tag{2.7}$$

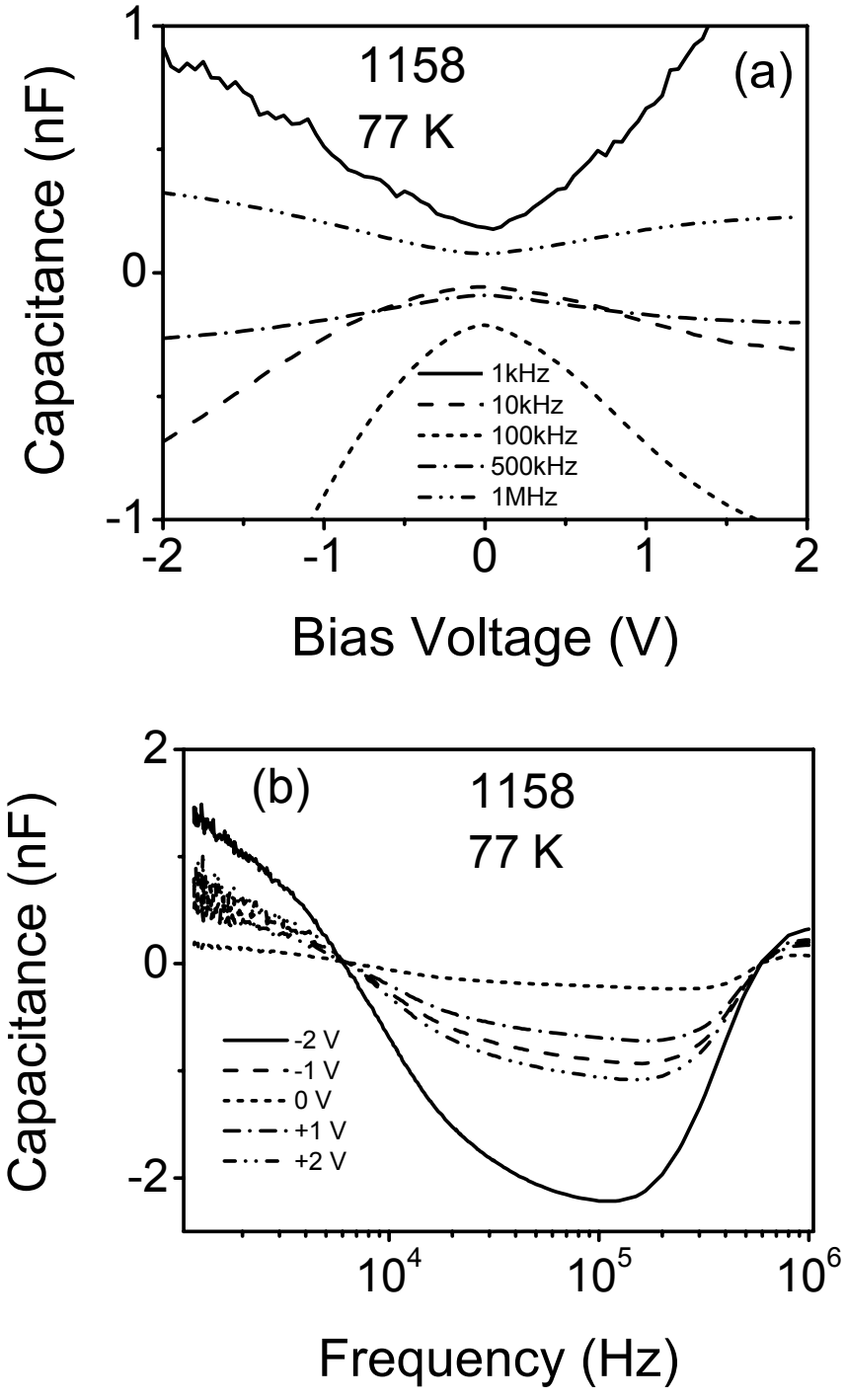

Figure 2.6: FDCD and negative capacitance were observed in both the (a) C-V profile and (b) C-f profile. From the C-f profile, inverse relaxation times of $\sim$1.77$\pm$0.05 and 155$\pm$9 μs were calculated from the points where the capacitance transitioned from negative to positive or positive to negative.

In eqn. 2.7, the sign of the second term is dependent on both frequency and the behavior of the transient relaxation current in the time-domain, specifically, the time-derivative. In response to a small voltage step ΔV, if $\delta j(t)$ exhibits positive-valued behavior (as reported [17] in cases of impact ionization of impurities and other interface effects) and the magnitude is greater than C_0, the integral in eqn. 2.7 will become negative, resulting in negative capacitance.

Frequency-dependent capacitance dispersion (FDCD) was observed in the C-V profiles, shown in Fig. 2.6(a), and has been attributed to the presence of frequency-dependent trap states. Such phenomena have been observed in the 10 kHz to 1 MHz regions of other GaN/AlGaN heterojunctions such as Schottky diodes [8] and heterojunction field effect transistors (HFETs). [16] In addition to FDCD, negative capacitance was observed in the C-V profiles of sample 1158 for frequency values of 10-500 kHz. Negative capacitance has been observed [15,18,19] in various other detector structures. The phenomenon has been attributed to carrier generation and recombination at interface defect states, most likely due to the presence of occupied trap states at the emitter/intrinsic layer interface. [15] Due to the symmetry in the C-V profiles for both forward and reverse biasing, it is assumed that the processes responsible for negative capacitance and FDCD are present at both heterointerfaces.

The band diagram, including the location of the defect states under zero bias, is depicted in Fig. 2.7(a). In the figure, the n^+-GaN TC is to the left of the intrinsic $Al_{0.0.26}Ga_{0.974}N$ barrier layer and the n^+-GaN BC is to the right; the diagram is intended to show the area between metal contacts. When a bias is applied across the device, as depicted in Fig. 2.7(b), electrons with sufficient energy will either surmount the barrier or fill up any available defect states at the emitter/barrier interface. However, under certain frequency and bias conditions, electrons that possess sufficient energy will be able to dislocate any electrons already present in trap states below

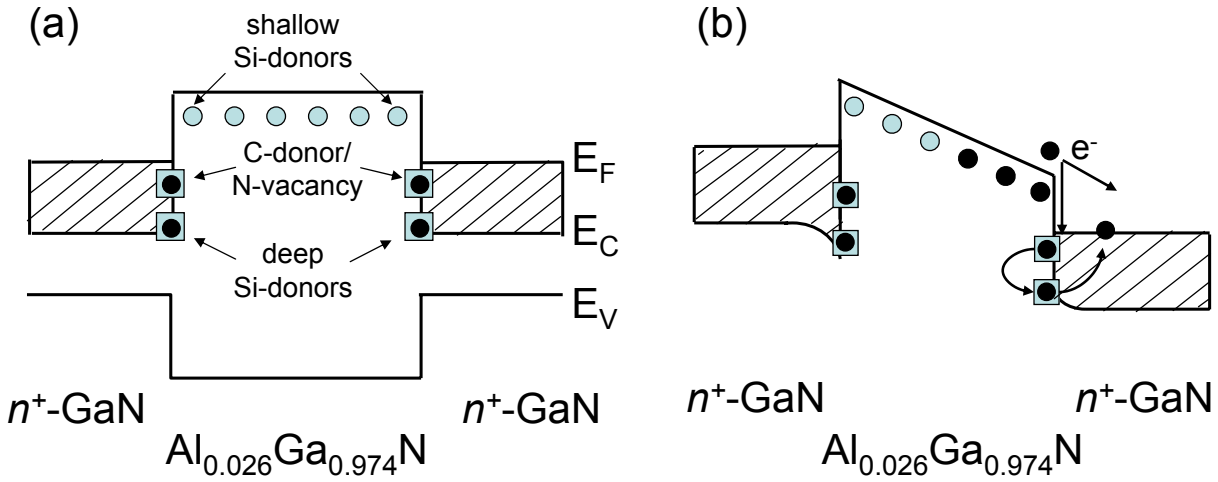

Figure 2.7: Band diagram for sample 1158 with (a) zero bias and (b) reverse bias. When the 1158 sample was reverse biased the C-donor/N-vacancy trap states were located below the Fermi level.

the Fermi level in a process similar to impact ionization or the Auger effect. These ionized trap states then act as electron recombination centers. In an n^+-doped semiconductor, the relaxation times of electron recombination centers below the Fermi level are faster than that of the trap states above the Fermi level due to the excess of available electrons. When the electron occupancy of states below the Fermi level exceeds the occupancy of electrons above the Fermi level, the interface charge density variation is reversed and capacitance becomes negative.

The negative capacitance observed in C-f profiles, shown in Fig. 2.6(b), allowed for the extrapolation of trap state relaxation times. The transition from positive to negative capacitance occurred around 6 kHz, while the transition from negative to positive capacitance was at ∼600 kHz. These two frequencies correlate to f^{-1} relaxation times of 155±9 and 1.77±0.05 μs, respectively. The faster relaxation time is attributed to trap states below the Fermi level, possibly C-donor/N-vacancy defect states and deep Si-donor states (pinned to the n^+-GaN emitter layer), and the slower relaxation time to defect states above the Fermi level, probably due to shallow Si-donor states in the $Al_{0.0.26}Ga_{0.974}N$ barrier layer. At frequencies less than 6 kHz both generation and recombination

processes are occurring; however, the dominant trap states (shallow Si-donor) are located above the Fermi level and consequently the capacitance is positive. At ∼6 kHz the trap states associated with a long relaxation time (slow trap states) are saturated and the electron recombination centers exhibiting short relaxation times (fast trap states) become dominant, thus, producing a negative capacitance. The fast trap states remain active until ∼600 kHz, above which these trap states also become saturated. Once both generation and recombination processes have become inactive, due to high frequency, the capacitance returned to a positive value and approached the geometrical capacitance of the sample.

In order to model the C-f profiles, the contributions from both majority and minority carriers are incorporated by including [17] both positive and negative exponential components into the transient response current. The corresponding capacitance calculated from eqn. 2.7 is then:

$$C(\omega) = C_0 + \frac{a_1}{1 + (\omega\tau_1)^2} - \frac{a_2}{1 + (\omega\tau_2)^2}. \tag{2.8}$$

where a_1 and a_2 are constants, and τ_1 and τ_2 are the relaxation times of the majority and minority carriers, respectively.

Relaxation times $\tau_1 = 140\pm20$ μs and $\tau_2 = 1.74\pm0.10$ μs, were found using eqn. 2.8 and were in agreement with the f^{-1} relaxation times from the C-f profiles. However, the amplitude of the C-f profiles could not be fit using a Debye relaxation model, indicating that non-Debye processes are active in the sample. In the high-frequency limit ($\omega \to \infty$), the capacitance will approach the geometric capacitance of the sample due to finite inertia of the carrier transport processes when both the faster and slower trap states can no longer respond.

Using the present experimental data, summarized in Table 2.1, a comprehensive model including defect trap states for an n^+-GaN/$Al_{0.0.26}Ga_{0.974}N$ heterostructure can be constructed. The fast trap states are tentatively assigned to C-donor/N-vacancy and deep Si-donor defect states

Table 2.1: Summary of experimentally obtained parameters and corresponding defect states. The activation energies were calculated from IR spectra transitional energies. Because the states below the Fermi level behave as a single defect state, the relaxation times are the same. The conduction band offset due to Si-donors (pinned to n^+-GaN) was calculated to be 137±7 meV.

Defect	Position	Optical $E_{activation}$	Relaxation times (μs) Exp.	Calc.
Shallow Si-donor	Above E_F (pinned to AlGaN)	30.8±0.2 meV	155±9	140±20
C-donor/N-vacancy	States below E_F	125±1 meV	1.77±0.05	1.74±0.10
Deep Si-donor	States below E_F (pinned to GaN)	140±2 meV	1.77±0.05	1.74±0.10

at the n^+-GaN/$Al_{0.0.26}Ga_{0.974}N$ heterointerface positioned below the Fermi level, while the slow trap states appear to be correlated with shallow Si-donor impurity states in the $Al_{0.0.26}Ga_{0.974}N$ barrier layer positioned above the Fermi level.

2.3.2 Effects of Etching Depth

Using dry etching techniques, three samples were processed to form square mesas with TC n^+-GaN emitter thicknesses of 0.2 μm (unetched), 0.02 μm (partially-etched), and 0 μm (fully-etched). A schematic of the three structures is shown in Fig. 2.8. Only the area inside the metal rectangular contact was etched, the n^+-GaN layer under the rectangular contact remained intact (0.2 μm thick). Thus, a small n^+-GaN/$Al_{0.026}Ga_{0.974}N$ heterojunction would still be present at the TC/barrier interface.

A trend was observed between the etching depth of the TC and capacitance characteristics. Under reverse biasing, the C-V profiles consistently showed FDCD independent of TC emitter thickness. However, with forward biasing, as the emitter thickness decreased (etching depth increased)

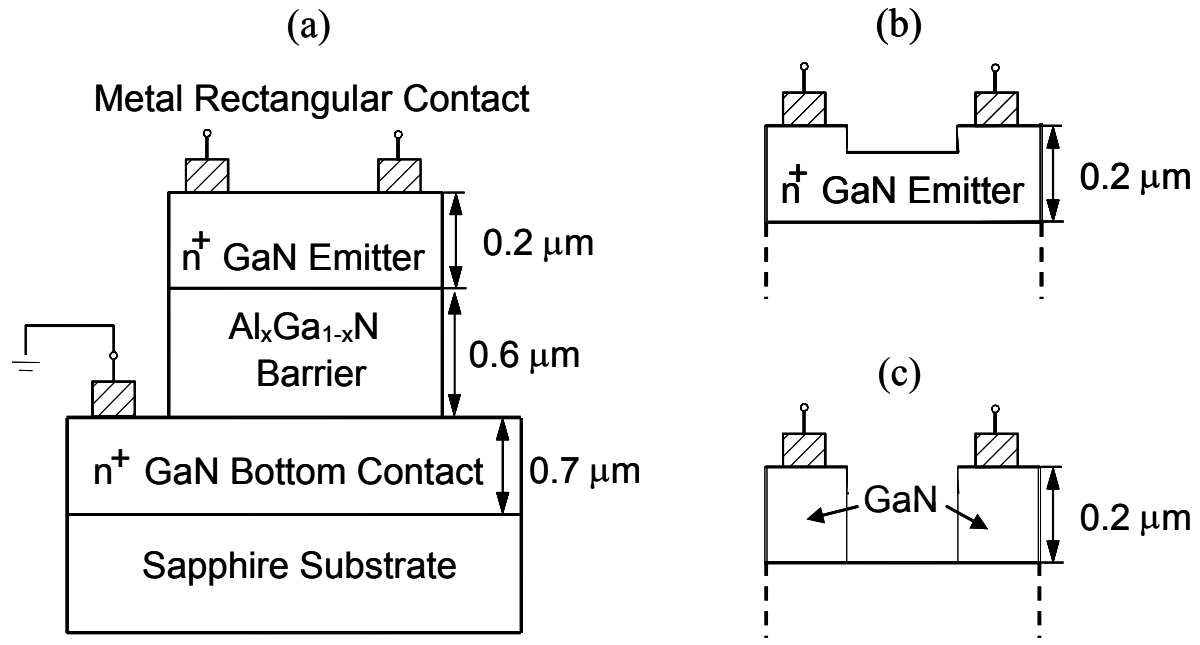

Figure 2.8: Structure of sample 1158 when (a) unetched, (b) partially-etched, and (c) fully-etched. Only the area between the metal contacts were etched, thus, even the fully-etched sample has a small heterointerface at the TC.

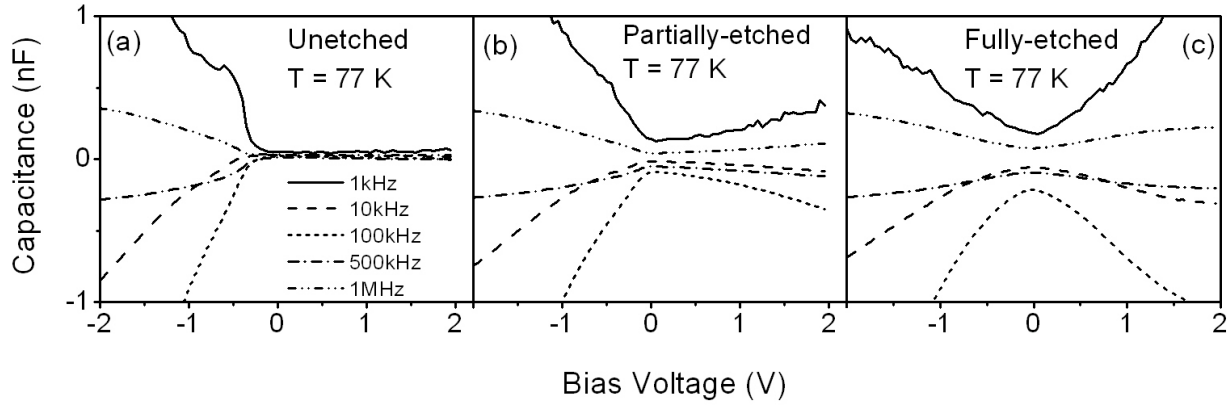

Figure 2.9: C-V profiles of the (a) unetched, (b) partially-etched, and (c) fully-etched samples. The degree of capacitance dispersion increased when forward biased as etching depth increased due to a secondary process that competes with the frequency-dependent trap states.

the capacitance dispersion increased, revealing that there is a secondary competing processes, which counteracts the effects of the frequency dependent trap states present at or in the vicinity of the TC/barrier heterojunction. The location and mechanism of the unknown competing process still needs further research, but is thought to result from sample processing. The unetched sample, shown in Fig. 2.9(a), exhibited FDCD only under reverse bias, but with forward bias the capacitance appeared to be independent of both frequency and bias. The asymmetry of FDCD between samples of different etching depths suggests that the frequency-dependent trap states, while present at both heterointerfaces, are the dominant trapping mechanism only at the BC/barrier interface ($Al_{0.026}Ga_{0.974}N/n^{+}$-GaN) heterointerface. The partially-etched and fully-etched samples showed FDCD for both forward and reverse bias, shown in Fig. 2.9(b) and (c). The partially-etched sample displayed moderate capacitance dispersion while the fully-etched sample was essentially symmetric for both forward and reverse bias. Others have reported [19] asymmetry in C-V profiles due to dopant migration.

Additionally, as etching depth increased, the negative capacitance became more pronounced, similar to the trend in FDCD. While it was expected that negative capacitance would occur in the unetched sample under forward bias, etching appeared to remove the additional process active at the TC/barrier interface, allowing the mechanism responsible for negative capacitance to be the dominant trapping mechanism at both heterointerfaces; hence, the C-V profiles for the fully-etched are symmetric.

2.4 Effects of Barrier Al Concentration

Variations in barrier layer Al content and contact layer doping concentration will change the UV and IR threshold. However, increased Al content has been found [8] to contribute to the

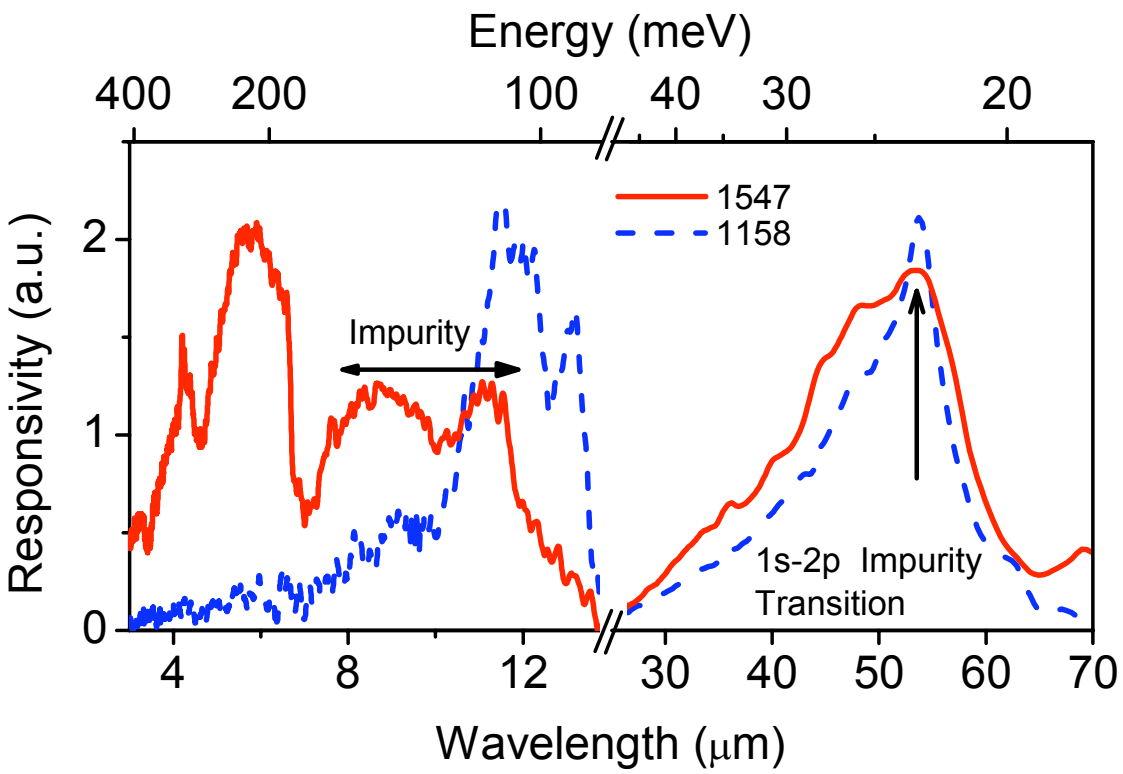

Figure 2.10: IR spectra showing the free carrier response peaks between 3-8 μm and 8-14 μm for sample 1547 and sample 1158, respectively. Defect related absorption centers with transitional energies of 112±0.5 and ∼142 meV (corresponding to activation energies of 149±1 and ∼189 meV, respectively) were observed in sample 1547 and attributed to C-donor/N-vacancy and deep Si-donor centers. In sample 1158 C-donor/N-vacancy and deep Si-donor defect states had transitional energies of 93.4±0.5 and 105±1.5 meV, corresponding to activation energies of 125±1 and 140±2 meV, respectively. Shallow Si-donor states in the $Al_xGa_{1-x}N$ barrier with $1s$-$2p_{\pm}$ transitional energy of 23.2±0.1 meV (sample 1547) and 23.1±0.1 meV (sample 1158) were observed in both samples.

number of interface defect states due to increased lattice strain at the heterojunction.

In the IR spectra of sample 1547 and sample 1158, shown in Fig. 2.10, free carrier response peaks are observed between 3-8 μm and 8-14 μm, respectively, consistent with the Al fractions of 0.1 and 0.026. A broad impurity related response peak is also present in the 8-13 μm range of sample 1547, as described in section 2.2. In sample 1158, defect related absorption peaks are observed superimposed on the free carrier response between 11 and 13.6 μm, as described in section 2.3. A summary of sample parameters and associated defect state energies is provided in Table 2.2.

For both samples, an absorption peak corresponding to a defect energy state with a 1s-

Table 2.2: Summary of sample parameters and defect related activation energies. In sample 1547, the C-donor/N-vacancy and shallow Si-donor defect states were located above the Fermi level, whereas in sample 1158, C-donor/N-vacancy and deep Si-donor defect states were located below the Fermi level.

	Sample Number	
	1547	1158
Al fraction	0.10±0.001	0.026±0.001
Work function (meV)	200±2	88±2
Conduction band offset (meV)	248±6	137±7
Free carrier response (μm)	3-8	8-13
Shallow Si-donor (meV)	30.9±0.1	30.8±0.2
C-donor/N-vacancy (meV)	149±1	125±1
Deep Si-donor (meV)		140±2
Unknown defect state (meV)	∼189	

2p± transitional energy of 23.2±0.1 meV (sample 1547) and 23.1±0.1 meV (sample 1158) was observed at ∼54 μm and attributed to shallow Si-donor impurities in the $Al_xGa_{1-x}N$ barrier layer. The presence of these trap states with almost identical activation energies indicates that while the barrier Al fraction changes the barrier height and location of interface trap states, it does not effect the location of the shallow Si-donor impurities in the $Al_xGa_{1-x}N$ barrier.

Both samples investigated show similar defect energy states, regardless of Al fraction. However, the response of the C-donor/N-vacancy and deep Si-donor related states to an applied bias, as observed in the C-V and C-f profiles, was different. Even though changes in Al fraction did not introduce new trap states, the conduction band offset was altered, changing the position of the Fermi level relative to the trap states.

The Al concentration of sample 1547 (0.1) resulted in a workfunction of 200 meV, positioning the Fermi level below the C-donor/N-vacancy trap states. Under an applied bias, the

Fermi level can be moved through the defect energy states causing abrupt changes in the carrier concentration, resulting in the observed capacitance-step and capacitance hysteresis. Due to the conduction band offset in sample 1547, calculated to be 248±6 meV, the deep Si-donor related states are pinned to the n^+-GaN layer and are therefore not active in the process responsible for the capacitance-step or capacitance hysteresis. Additionally, because of the large energy difference between the deep Si-donor states (below E_F) and the C-donor/N-vacancy, negative capacitance does not occur, even when the C-donor/N-vacancy states are below the Fermi level.

Due to the low Al fraction in sample 1158 (0.026), the workfunction was reduced to 88 meV, resulting in the Fermi level lying above the C-donor/N-vacancy and deep Si-donor trap states. Since the Fermi level consistently remained above the trap states, these defect energy states were always occupied, and no abrupt change in carrier concentration occurred. Thus, no capacitance-step or capacitance hysteresis was observed. However, negative capacitance was observed in both the C-V and C-f profiles of sample 1158 due to an impact ionization-like process between the trap states at the heterointerface, below the Fermi level.

To confirm that the negative capacitance displayed by sample 1158 was due to the presence of defect states below the Fermi level, and not shallow Si-donor trap states in the $Al_{0.026}Ga_{0.974}N$ barrier layer, a similar n^+-GaN/$Al_{0.1}Ga_{0.9}N$ sample (sample 1547) was used to obtain thermal activation energies. Sample 1547 has the same Si doping concentration (5×10^{18} cm^{-3}) and shallow Si-donor activation energy (from IR spectra) as sample 1158. Because sample 1547 did not exhibit negative capacitance an Arrhenius plot, shown in Fig 2.11, could be constructed using C-f relaxation times. A thermal activation energy of 15±1 meV was extracted from an Arrhenius plot at temperatures ranging from 50 to 110 K. Other groups reported [24] similar thermal activation energies of 12-17 meV for shallow Si-donor impurities in GaN.

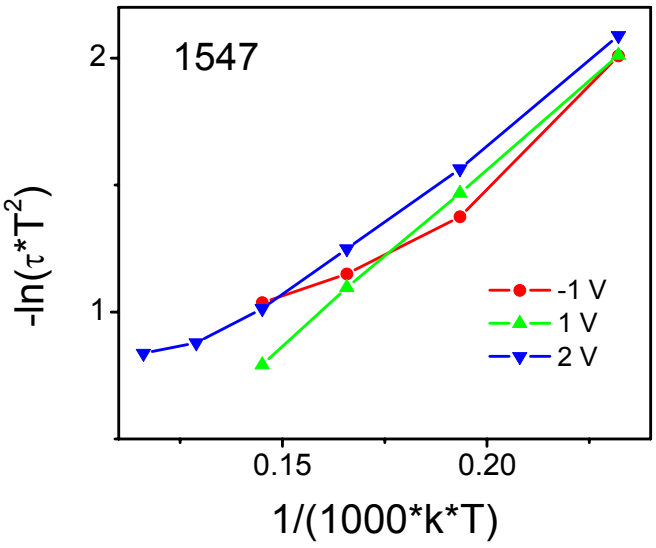

Figure 2.11: Thermal activation energies of 15±1 meV were obtained from an Arrhenius plot of sample 1547.

The energy difference of approximately 16±1 meV between the Si-donor activation energy estimated by IR spectroscopy and the thermal activation energy obtained from the Arrhenius plot indicates that shallow Si-donors contribute to carrier transport through both thermionic emission and thermally-assisted tunneling due to barrier thinning. The discrepancy between these two activation energy values is due to the fact that an Arrhenius plot provided the thermal activation energy required for the particle to reach an excited bound-state energy level where thermally-assisted tunneling could take place through the potential barrier. In the case of thermally-assisted tunneling, the activation energies obtained by an Arrhenius plot will therefore be lower than the activation energies obtained by IR spectroscopy, as observed here.

Chapter 3

n^+-GaN/$Al_{0.026}Ga_{0.974}N$/i-GaN/n^+-GaN Dual-band Detectors (3-Contact)

Dual-band UV/IR detection takes place using separate UV- and IR-active layers, as depicted in Fig. 3.1. UV response occurs when a UV photon is absorbed in the $Al_xGa_{1-x}N$ barrier layer, generating an electron-hole pair. The carriers are then swept out by an external electric field and collected at the contacts. IR response results from intraband transitions due to free carrier absorption in the n^+-GaN layer. The photoemitted electrons are then transported through the barrier layer and collected at the contacts. When separate UV-active and IR-active regions are used (with a common contact layer), UV/IR detection can occur independently or simultaneously within a single structure.

3.1 Device Growth and Processing

The 3-contact n^+-GaN/$Al_xGa_{1-x}N$/i-GaN/n^+-GaN UV/IR dual-band detectors were grown by low pressure Metal-Organic Chemical Vapor Deposition (MOCVD) on a c-plane sapphire substrate. The 3-contact structure, is a UV-active region on top of a IR-active barrier layer, thus,

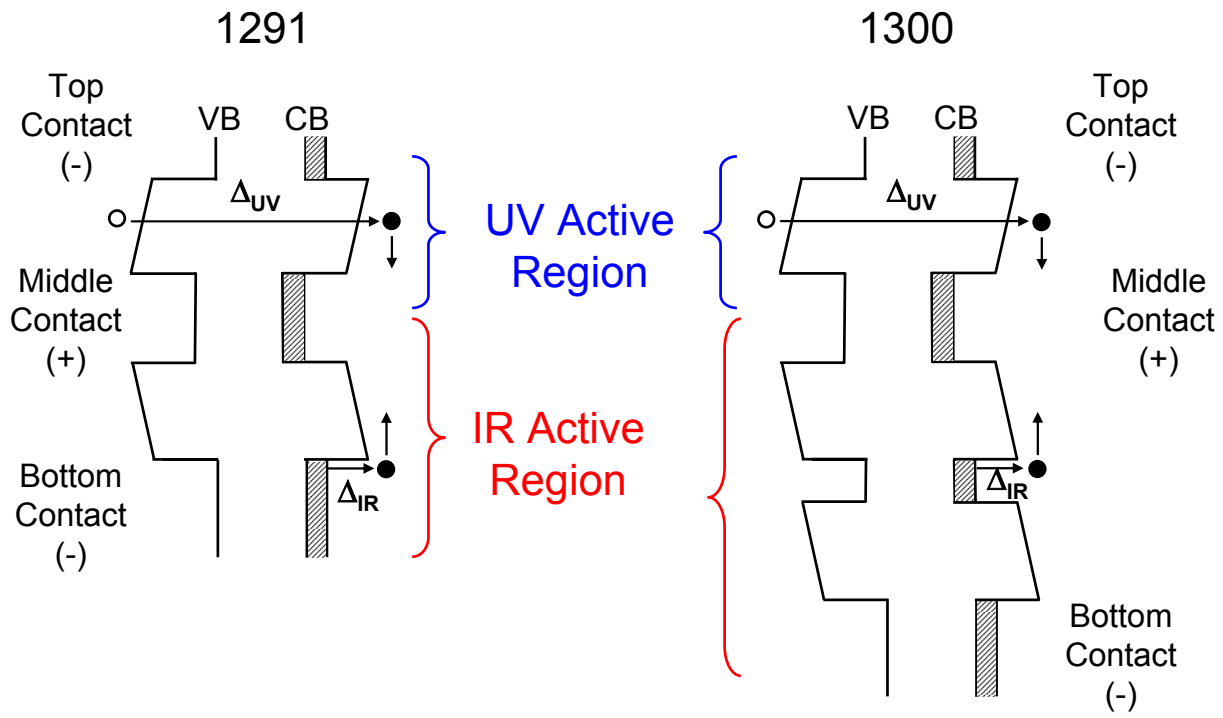

Figure 3.1: Schematic of the dual-band detection mechanism for the (a) 1291 structure and the (b) 1300 structure. Dual-band UV/IR detection can occur independently or simultaneously within a single structure when separate UV- and IR-active layers are included. UV response is due to electron-hole generation in the $Al_{0.026}Ga_{0.974}N$ barrier layer, while IR response is due to intraband photoexcitation of an electron in the GaN emitter layer.

allowing for simultaneous dual-band detection. In the 1291 samples there is a single UV-active region on top of a single barrier IR-active barrier region, whereas the 1300 samples have a single UV-active region on top of a double-barrier IR-active region. The UV-active region consists of a 0.1 μm n^+-GaN top-contact (TC) layer, a 0.35 μm $Al_{0.026}Ga_{0.974}N$ UV-active barrier layer, 0.15 μm i-GaN buffer layer, and an 0.6 μm n^+-GaN middle-contact (MC) layer. Below the UV-active region is an IR-active region consisting of a 0.35 μm $Al_{0.026}Ga_{0.974}N$ barrier layer, another 0.15 μm i-GaN buffer layer, followed by the 1 μm n^+-GaN bottom-contact (BC) layer. For the 1300 samples, there is an additional 0.05 μm n^+-GaN layer, a 0.35 μm $Al_{0.026}Ga_{0.974}N$ layer, and a 0.15 μm i-GaN layer. All n^+-GaN layers are Si-doped to a concentration of 5×10^{18} cm^{-3}. When considering the TC-MC layers independent of the MC-BC layers, the structure is similar to the 1158 samples, and was expected to give similar response.

The i-GaN layer in the 3-contact samples introduces a homojunction at the i-GaN/n^+-GaN interface. Due to dopant migration, the Si induced defect bands and discrete Si-donor states are present in the i-GaN barrier, pinned to the n^+-GaN layer. This energy band coincides with the conduction band minimum of the n^+-GaN layer.

Dry etching techniques were used to form square mesas on all samples, and in some cases remove the UV-active region. The structures were processed in the following ways:

- Sample 1291-1 has only the UV-active region TC-MC wired.
- Sample 1291-2 has the UV-active region fully etched away and only the IR-active region MC-BC wired.
- Sample 1300-1 has the UV-active region fully etched away and only the IR-active region MC-BC wired.

- Sample 1300-2 has only the UV-active region TC-MC wired.
- Sample 1300-3 has both the UV- and IR-active regions wired.

A schematic of the post processing structure of the 1291 samples and the 1300 samples are depicted in Fig. 3.2 and Fig. 3.3, respectively.

Sample 1291-1 and sample 1300-2 were wired TC-MC so that only the UV-active region was measured. When only the UV-active region was wired, the effective structure consisted of a n^+-GaN MC, an i-GaN barrier, an intrinsic $Al_{0.026}Ga_{0.974}N$ barrier, and a n^+-GaN TC.

The n^+-GaN TC, $Al_{0.026}Ga_{0.974}N$ barrier, and i-GaN layer in sample 1291-2 were fully etched away so that only the IR-active MC-BC contacts were present. In this sample the structure was similar to the TC-MC, consisting of a n^+-GaN BC, an i-GaN barrier, an intrinsic $Al_{0.026}Ga_{0.974}N$ barrier, and a n^+-GaN MC. In sample 1300-1, when the n^+-GaN TC, $Al_{0.026}Ga_{0.974}N$ barrier, and i-GaN layer were etched away, the structure consists of a n^+-GaN BC, an i-GaN barrier, two intrinsic $Al_{0.026}Ga_{0.974}N$ barrier with an n^+-GaN layer between, and a n^+-GaN MC.

3.2 C-V Measurements

Capacitance-voltage (C-V) and capacitance-frequency (C-f) measurements were carried out using a computer-controlled Hewlett Packard 4284A LCR meter. Generally, C-V-f scans show electrical characteristics of the interface closest to the emitter. However, processes responsible for negative capacitance occur at the interface closest to the contact where carriers are collected. When forward biased, the TC of sample 1291-1 was positive and the MC negative; whereas for sample 1291-2, the MC was positive and the BC was negative. Under reverse bias, the polarity of both samples is the opposite.

It was expected that sample 1291-1, sample 1291-2, and sample 1300-2 would display

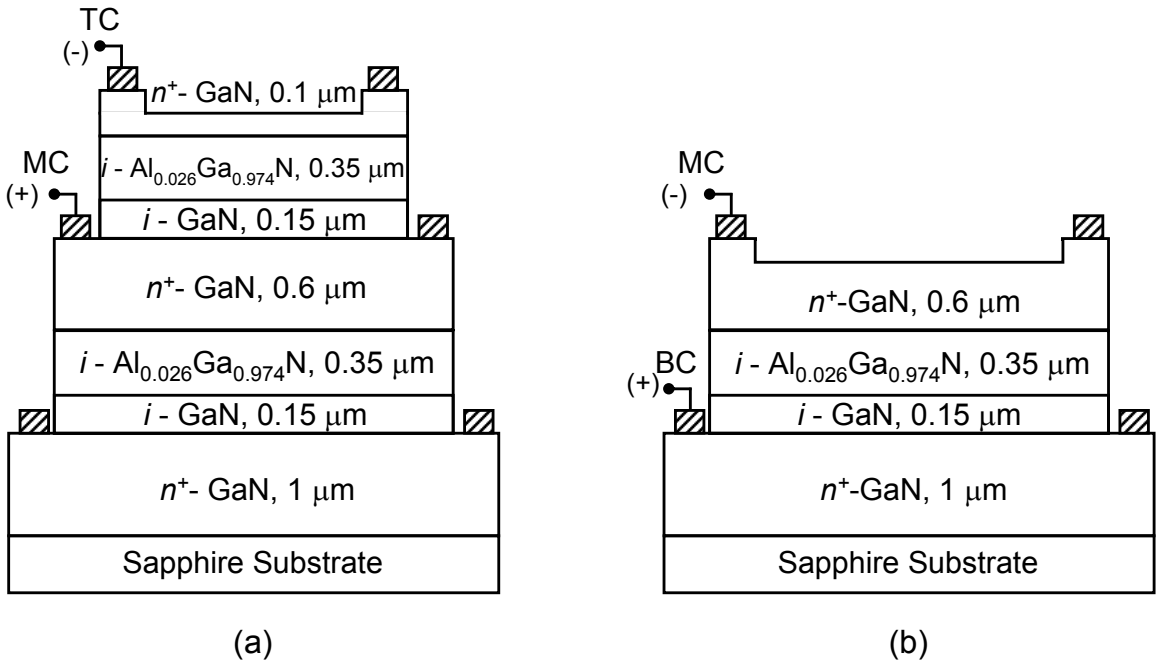

Figure 3.2: Post-processing structures of (a) sample 1291-1 and (b) sample 1291-2. Sample 1291-1 was wired (TC-MC) so that only the UV-active region was measured. The n^+-GaN TC, $Al_{0.026}Ga_{0.974}N$ barrier, and i-GaN layer in sample 1291-2 were fully etched away so that only the IR-active MC-BC layers were present.

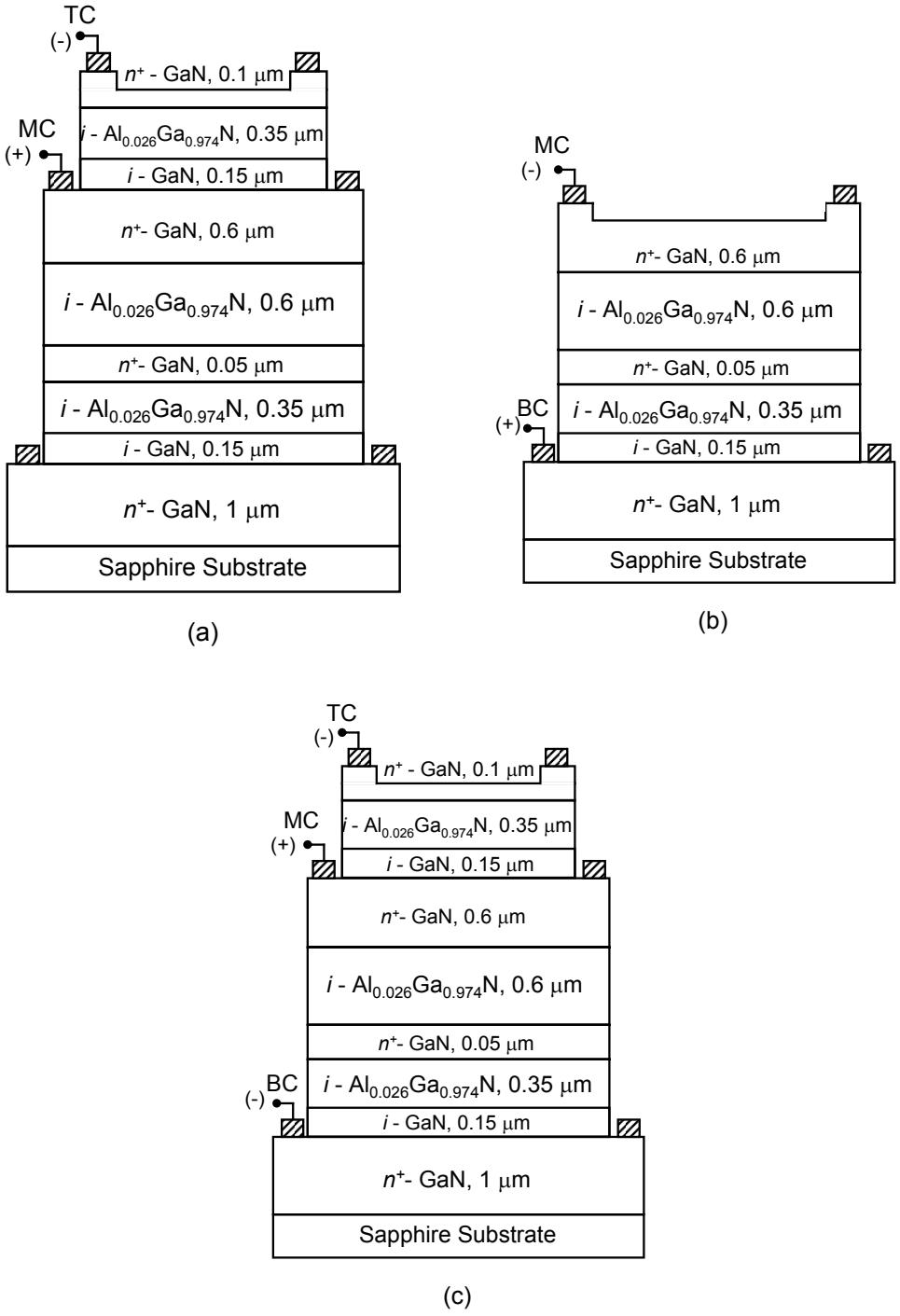

Figure 3.3: Post-processing structures of (a) sample 1300-2 with TC-MC wired so that only the UV-active region was measured. (b) In sample 1300-1, the UV-active region was fully etched away, leaving only the IR-active region (BC-MC). (c) Both UV and IR active regions (TC-MC-BC) were wired in sample 1300-3.

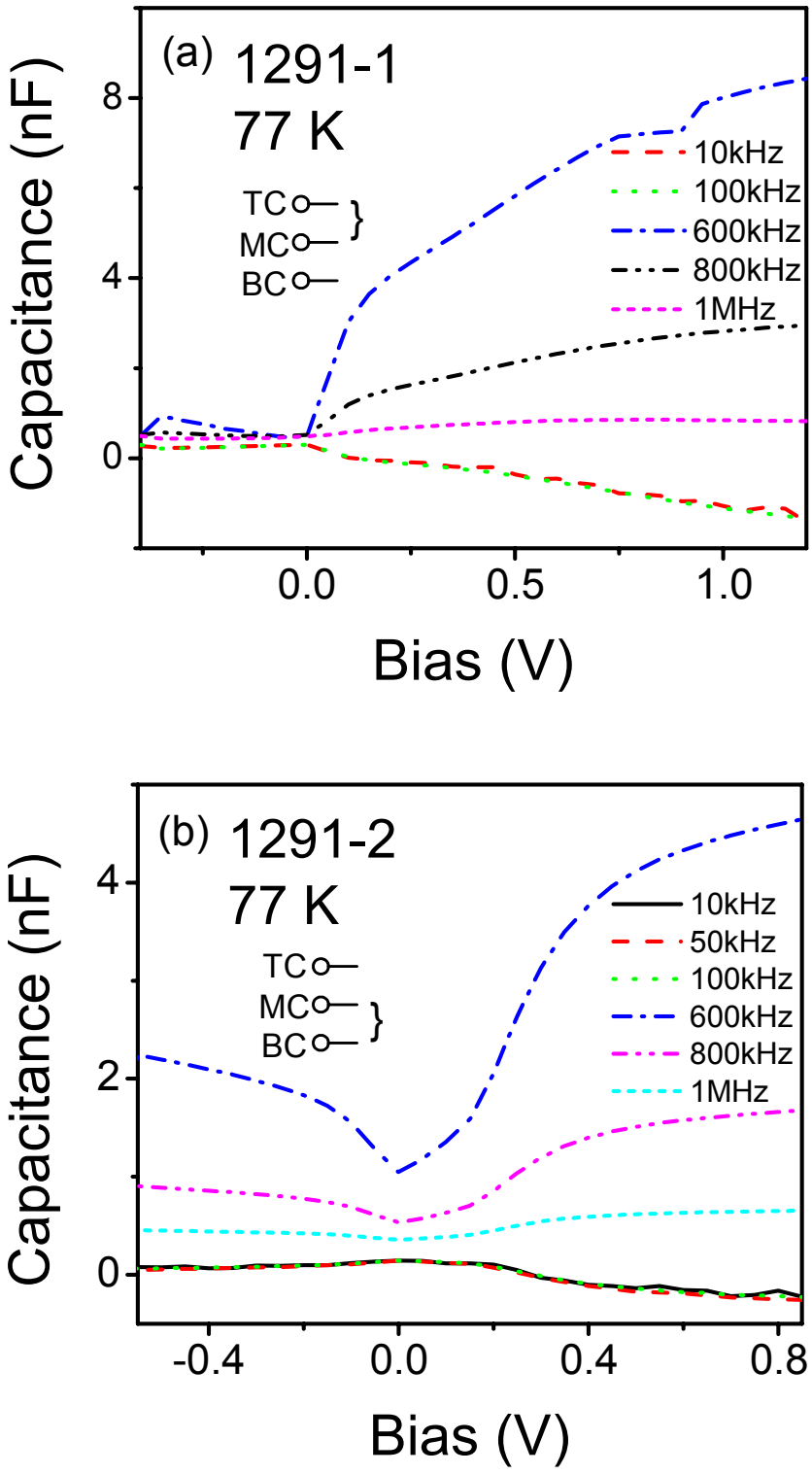

Figure 3.4: C-V profile of (a) sample 1291-1 (TC-MC) showing FDCD when the sample was forward biased, but not when reverse biased. The asymmetry is due to etching effects. (b) C-V profile of sample 1291-2 (MC-BC) showed very little asymmetry.

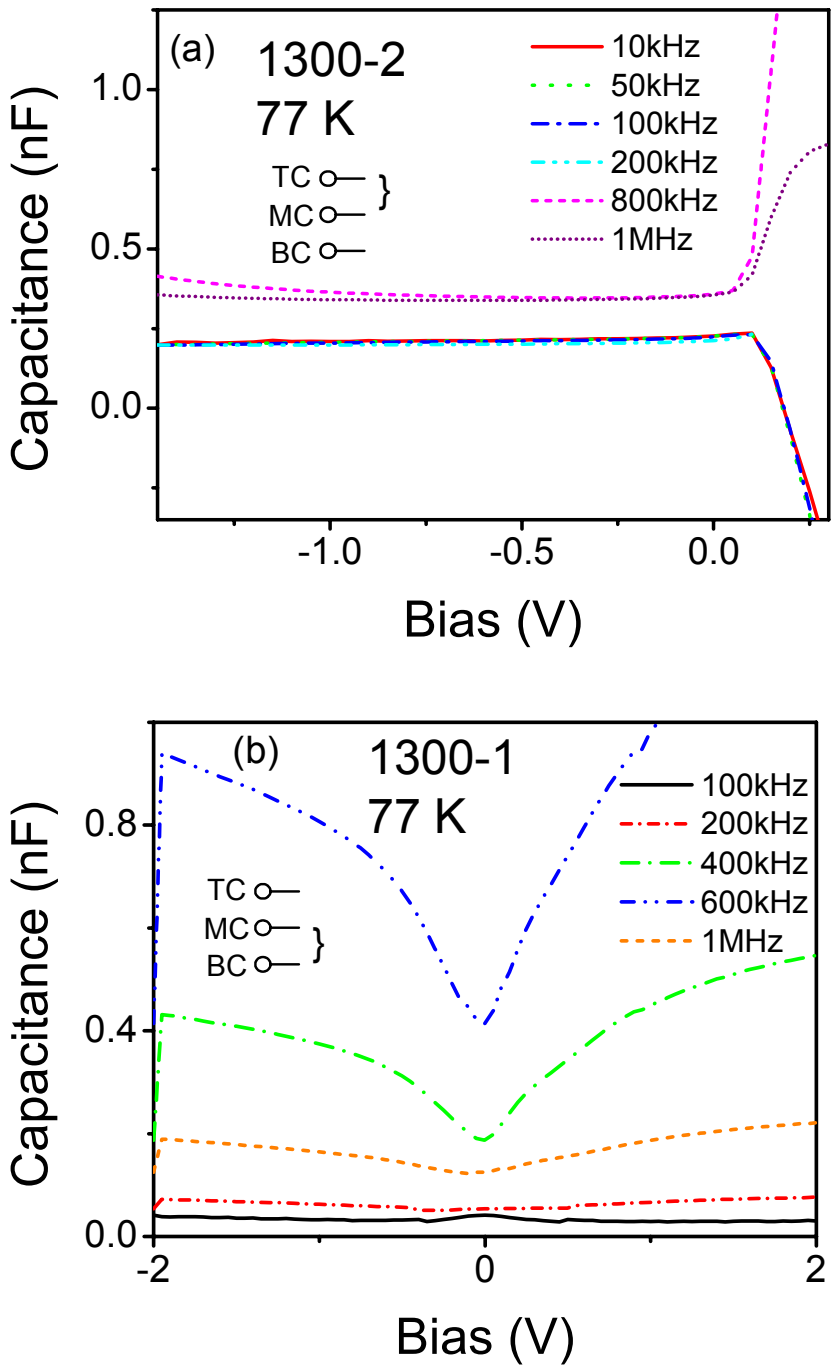

Figure 3.5: C-V profile of (a) sample 1300-2 (TC-MC) showing asymmetry and (b) sample 1300-1 (MC-BC) showing symmetric FDCD. Negative capacitance was observed in (a) under forward bias.

similar capacitance characteristics to the 1158 samples as the structures, were identical, with the exception of the i-GaN layer. In the C-V profile of sample 1291-1, Fig. 3.4(a), significant FDCD is only observed under forward bias. The strong asymmetry in the C-V profile between forward and reverse bias is expected as the interfaces at the $Al_{0.026}Ga_{0.974}N$ barrier are asymmetric. FDCD was observed in sample 1291-2 under both forward and reverse bias, as shown in Fig. 3.4(b). The C-V profile of sample 1291-1 resembled that of the unetched 1158 samples, whereas the C-V profile of sample 1291-2 resembled that of the partially-etched 1158 sample. This asymmetry is most likely due to processing issues, as discussed in section 2.3.2. Negative capacitance was observed for frequencies between 10 and 100 kHz in both sample 1291-1 and sample 1291-2 under forward bias. Additionally, there is no FDCD in the C-V profiles for frequencies exhibiting negative capacitance.

The UV-active TC-MC layer of the 1300-2 sample, had C-V characteristics similar to sample 1158, including asymmetric FDCD and negative capacitance. Fig. 3.5(a) shows the FDCD when sample 1300-2 was forward biased, while under reverse bias the capacitance is almost unaffected by frequency variations. Additionally, negative capacitance is present under forward bias between 10 and 400 kHz. The C-V profiles of sample 1300-1 (MC-BC), an example is provided in Fig. 3.5(b), were symmetric under forward and reverse bias, indicating that defect states are present a both interfaces. This symmetry is consistent with the C-V profiles of the fully-etched sample 1158 which is expected as the UV-active layer was etched away. FDCD can be observed in sample 1300-1, but no negative capacitance was seen.

3.3 High-Frequency Capacitance Peak

An anomalous high-frequency capacitance peak was observed in the C-f profiles for the 3-contact samples, shown in Fig. 3.6 and Fig. 3.7. When the samples are unbiased or reverse biased,

a high-frequency peak is observed, the amplitude of which increased with increasing bias. With forward biases, the high-frequency peak is present, but discontinuous between ∼150 and 400 kHz due to limitations of the LCR meter. Additionally, negative capacitance was observed, most likely due to deep Si-donor states at the n^+-GaN/$Al_{0.026}Ga_{0.974}N$ heterointerface. The capacitance transitioned from positive to negative at ∼2 kHz, and transitioned from negative to positive capacitance at a frequency within the discontinuity.

A broad free carrier peak was observed in the IR spectra of the 1291 samples and the 1300 samples, shown in Fig. 3.8 and Fig. 3.9, respectively, at ∼10.5 μm, consistent with the $Al_xGa_{1-x}N$ barrier Al fraction of 0.026. Additionally, defect related response peaks were observed between 11.5 and 13.5 μm and attributed to C-donor/N-vacancy and deep Si-donor defect states. For the 1291 samples, C-donor/N-vacancy and deep Si-donor defect states were observed with transitional energies of 94.2±0.5 and 104±1 meV, corresponding to activation energies of 125±1 and 139±2 meV, respectively; whereas, for the 1300 samples, the defect states have transitional energies of 94.3±0.5 and 102±1 meV, corresponding to activation energies of 125±1 and 136±2 meV, respectively. The high-frequency peak in the C-f profiles of the 3-contact samples could be due to a resonance effect involving the same trap states responsible for the negative capacitance observed in sample 1158.

Negative capacitance was attributed to an impact ionization-like process occurring at the n^+-GaN/$Al_{0.026}Ga_{0.974}N$ heterointerface due to C-donor/N-vacancy and deep Si-donor states. In the 2-contact structure (sample 1158), the capacitance transitioned from negative to positive at ∼600 kHz, corresponding to an inverse relaxation time of 1.77±0.05 μs and was attributed to Si-donor defect states below the Fermi level, pinned to the n^+-GaN layer. However, sample 1158 did not exhibit a high-frequency capacitance peak because the deep Si-donor states are located at the n^+-GaN/$Al_{0.026}Ga_{0.974}N$ heterointerface, and no homojunction is present. In the 3-contact

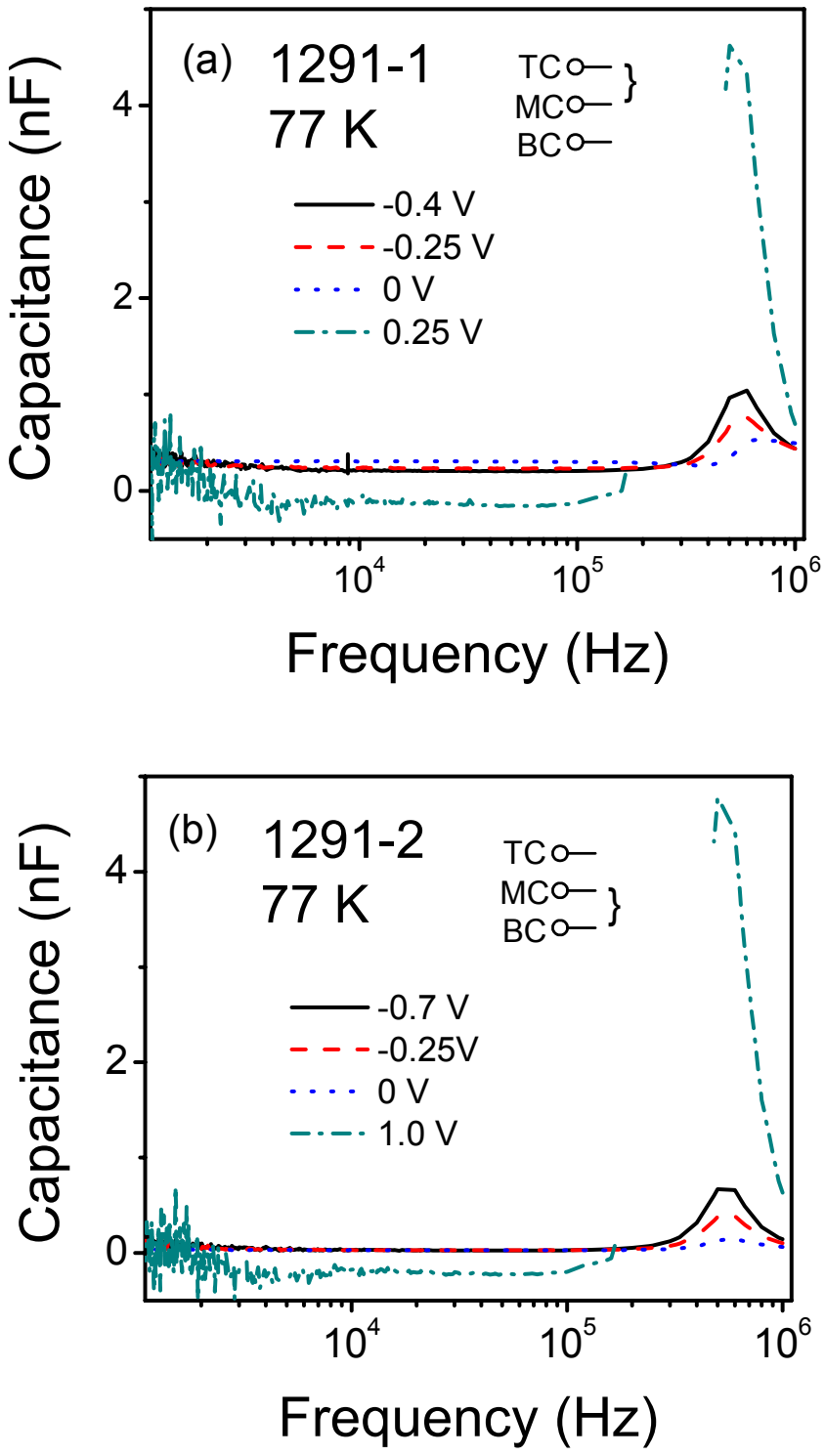

Figure 3.6: C-f profiles of (a) sample 1291-1 (TC-MC) and (b) sample 1291-2 (MC-BC) showing a high-frequency capacitance peak. The high-frequency capacitance peak is thought to be caused by resonant effects from Si-donor defect states at the i-GaN/n^+-GaN interface. In both samples, negative capacitance was observed for forward bias, and thought to result from an impact ionization-like process at the n^+-GaN/$Al_{0.026}Ga_{0.974}N$ interface. The discontinuity is due to the maximum capacitance limit of the LCR meter.

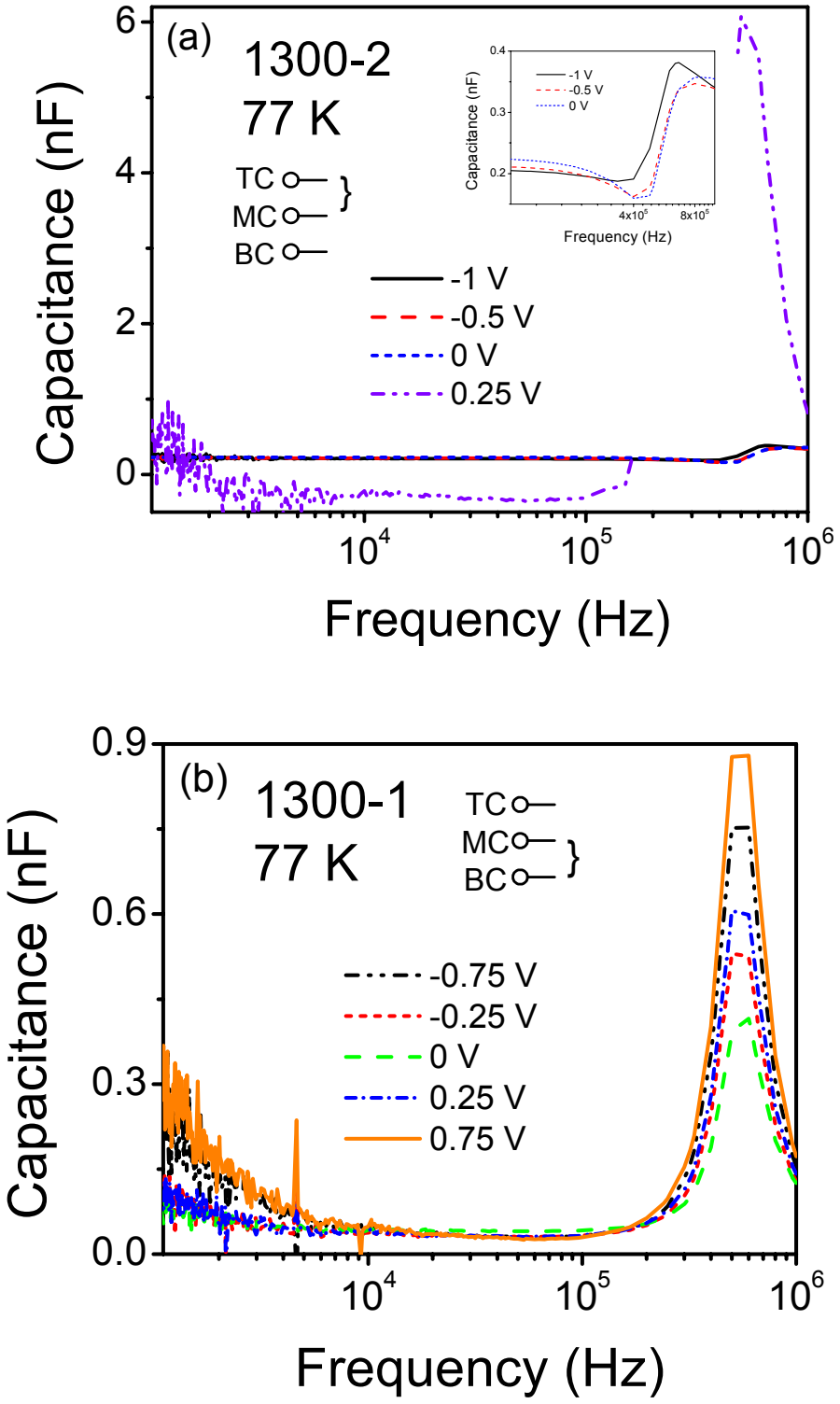

Figure 3.7: C-f profile of (a) sample 1300-2 (TC-MC) and (b) sample 1300-1 (MC-BC) showing a high-frequency capacitance peak. The peak is thought to be due to resonant effects at the interface trap states. For clarity, the inset to (a) shows a close-up of -1, -0.5, and 0 V between 100 kHz and 1 MHz.

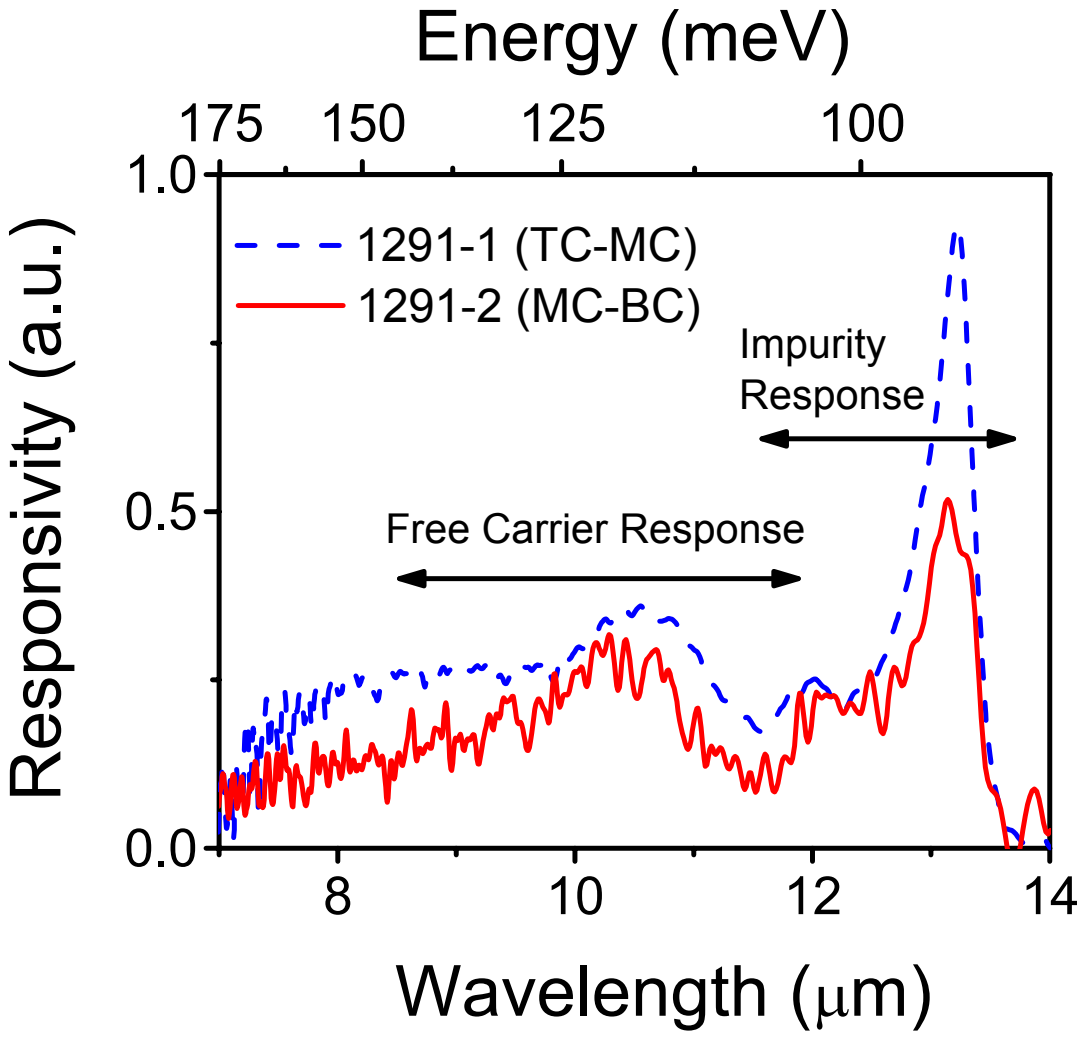

Figure 3.8: IR spectra of sample 1291-1 and sample 1291-2 showing a broad free carrier response peak at ∼11 μm, in addition to impurity related response between 12 and 13 μm. The defect related absorption centers with transitional energies of 94.2±0.5 and 104±1 meV were attributed to C-donor/N-vacancy and deep Si-donor states with activation energies of 125±1 and 139±2 meV, respectively.

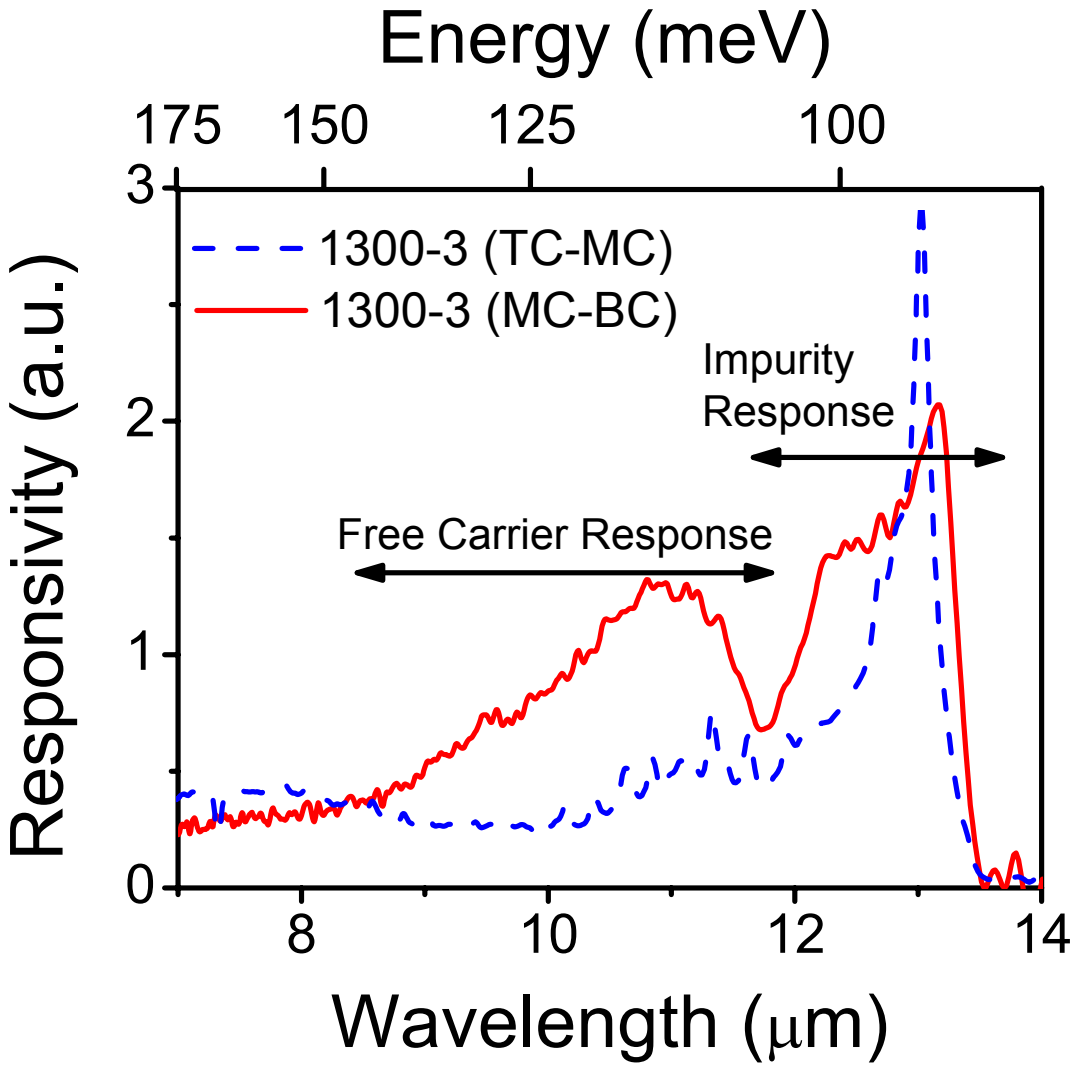

Figure 3.9: IR spectra of sample 1300-3. A broad free carrier response is seen with a peak at ∼11 μm. The arrow indicates the location of impurity absorption centers between 12 and 13 μm. The defect related absorption centers with transitional energies of 94.3±0.5 and 102±1 meV were attributed to C-donor/N-vacancy and deep Si-donor states with activation energies of 125±1 and 136±2 meV, respectively.

samples, there is a small i-GaN layer between the $Al_{0.026}Ga_{0.974}N$ barrier and n^+-GaN contact layer. Thus, the deep Si-donor induced defect states (pinned to the n^+-GaN layer) can exist in the i-GaN layer at the homojunction, in addition to the n^+-GaN/$Al_{0.026}Ga_{0.974}N$ heterointerface.

3.3.1 Complex Relaxation Time

To explain the resonance phenomenon responsible for the high-frequency capacitance peak, the complex capacitance and permittivity should be considered.

$$\tilde{C}(\omega) = (A/d)\tilde{\epsilon}(\omega) = C'(\omega) - iC''(\omega) \tag{3.1}$$

where

$$\tilde{\epsilon}(\omega) = \epsilon'(\omega) + \epsilon''(\omega) \tag{3.2}$$

For Debye relaxation, τ is assumed to be real, and the relaxation function is:

$$\phi(t) = \exp[-t/\tau]. \tag{3.3}$$

The corresponding capacitance function (after transformation into the frequency domain) is:

$$C(\omega) \propto \frac{1}{\cosh(\omega\tau)} \propto \frac{1}{1+\omega^2\tau^2} \tag{3.4}$$

where the right side is the Taylor expansion of $C(\omega)$ to second order. When both positive and negative exponential components are included [17] (in order to account for both majority and minority carrier), the capacitance can be modeled as:

$$C(\omega) = C_0 + \frac{a_1}{1+(\omega\tau_1)^2} - \frac{a_2}{1+(\omega\tau_2)^2}. \tag{3.5}$$

where C_0 is the geometric capacitance, a_1 and a_2 are constants, τ_1 and τ_2 are the relaxation times of the majority and minority carriers, respectively.

However, for non-Debye relaxation, τ can be complex valued, [29] where

$$\tau^{\star} = \tau' - i\tau''. \tag{3.6}$$

τ' and τ'' are the real and imaginary values of the complex relaxation time, respectively. The relaxation function then becomes:

$$\phi^{\star}(t) = \exp[-t/\tau^{\star}] \tag{3.7}$$

When the complex relaxation time $\tau^{\star}$ is substituted for τ, the expression for capacitance becomes,

$$C(\omega) \propto \frac{1}{\cosh(\omega\tau^{\star})} \propto \frac{1}{\cos[\omega(\tau' - \tau'')]} \tag{3.8}$$

Taylor expansion of the above expression to second order yields,

$$C(\omega) \propto \frac{1}{1 - \omega^2(\tau' - \tau'')^2} \tag{3.9}$$

The function is discontinuous when $\cos[\omega(\tau' - \tau'')] = 0$, corresponding to the observed high-frequency capacitance peak.

A Monte Carlo simulation, similar to that developed to explain the negative capacitance seen in sample 1158, was used to model the high-frequency capacitance peak. It was found that the peak could be generated using the equation similar to eqn. 3.5:

$$C(\omega) = C_0 + \frac{a_1}{1 + \omega^2\tau_1^2} - \frac{a_2}{1 - \omega^2({\tau_2}' - {\tau_2}'')^2}. \tag{3.10}$$

where C_0 is the geometric capacitance, a_1 and a_2 are constants, and τ_1 is the relaxation times of the majority carriers. In this case, the minority carries have a complex relaxation time $\tau_2^{\star} = {\tau_2}' - i{\tau_2}''$ where ${\tau_2}'$ and ${\tau_2}''$ are the real and imaginary part of $\tau_2^{\star}$, respectively. The essential difference in this equation as compared to eqn. 2.8, is the negative sign in the denominator of the last term (contribution from minority carriers). The negative sign will allow for a pole at $1 = \omega^2({\tau_2}' - {\tau_2}'')^2$, which is observed as the high frequency capacitance peak.

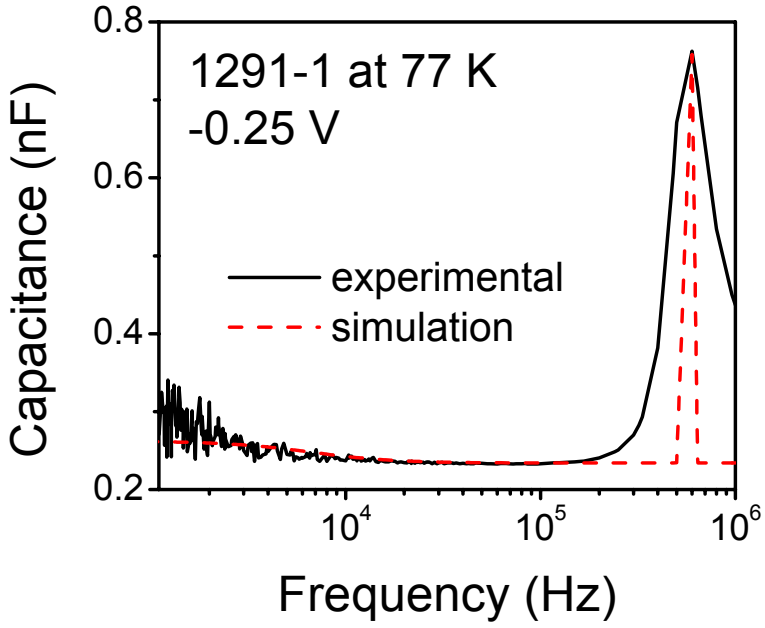

Figure 3.10: Monte Carlo simulation of sample 1291-1 along with the experimental plot. For this sample, τ_1 is 150.9 μs and $\tau_2{}'$ is 1.666 μs.

Based on the Monte Carlo simulation, $\tau_2{}'$ has a value between 1.67 μs and 2 μs, depending on the sample studied. A comparison between the experimental and simulation C-f profiles of sample 1291-1 are shown in Fig. 3.10. The high-frequency capacitance peak could only be recreated if $\tau_2{}'$ is equal to 1.666 μs. Because the minority carrier relaxation time from sample 1158 ($\sim$1.77 μs) falls within this range, it is assumed that the same trap state is active in both structures. The difference between $\tau_2{}'$ and $\tau_2{}''$ (obtained from the simulation) is $\sim$0.33 μs, which is consistent with the value of 0.442 μs calculated from eqn. 3.9.

3.3.2 Hybridization of Deep Si-donor Sites and Resonance Scattering

In semiconductors, there are three possible locations for the electronic energy levels of substitutional donor impurities: (i) discrete, bound energy states in the band gap, (ii) electronic energy levels lying in the valence band, and (iii) electronic energy levels lying in the conduction band. In cases (ii) and (iii), hybridization can occur between electrons from the impurity's ionic

core with the semiconductor's valence and conduction band, respectively. [25]

Multiple types of Si-donor states have been found [26] to exist in AlGaN and GaN systems, due to the stability of the Si_{Ga} configuration, as opposed to Si_N or Si-interstitial sites. [27] These states are located ∼30-40 meV below the conduction band edge. [20,21] Additionally, localized (metastable) states can form. In GaN, the localized state can be resonant with the conduction band; whereas in AlGaN, the localized state is present within the band gap. [26] This situation is analogous to case (iii) mentioned above.

It is thought that resonance scattering, due to the aforementioned Si-donor states, provides the mechanism necessary to explain the anomalous capacitance profiles, as resonance effects have previously been found [25] to alter the electrical characteristics of semiconductors. Resonance scattering has been found [25] to occur when (i) the ground state of the donor impurity lies within the band gap and (ii) the donor impurity has higher energy levels lying within the conduction band, leading to the delocalization of impurity electrons. Hybridization of the impurity site with the band induces virtual electron transitions [28] between a localized Si state and continuous conduction band states, leading to a resonance donor energy state. [25]

A schematic of the band diagrams under zero bias is depicted in Fig. 3.11, the band diagrams with forward and reverse bias is shown and Fig. 3.12. At zero bias, most electrons from localized Si-donors are in the ground state; but some will be in higher energy states due to thermal excitation. When a bias is applied, the excited localized states hybridize with continuous states in the conduction band. Under reverse bias, some resonance occurs at the homojunction, resulting in capacitance peaks with lower amplitude and no discontinuities.

When forward biased, negative capacitance was observed due to an impact ionization-like process at the n^+-GaN/$Al_{0.026}Ga_{0.974}N$ heterointerface and will only be observed if the process is

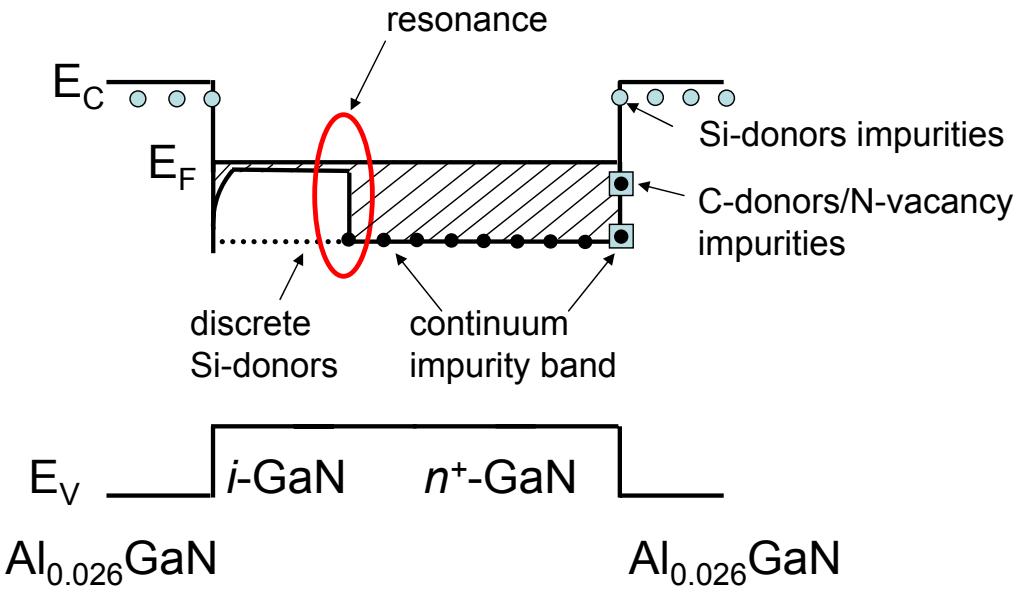

Figure 3.11: Location of the defect related trap states in the 3-contact structure. Resonance scattering can occur due to hybridization of the bound state levels of the deep Si-donor impurities in the band gap with excited states in the conduction band. Only the TC-MC layer is shown as it is expected that the MC-BC layer is similar.

occurring at the interface closest to the contact where carriers are collected. Resonance was much stronger under forward bias and the peak in capacitance has higher amplitude and discontinuities.

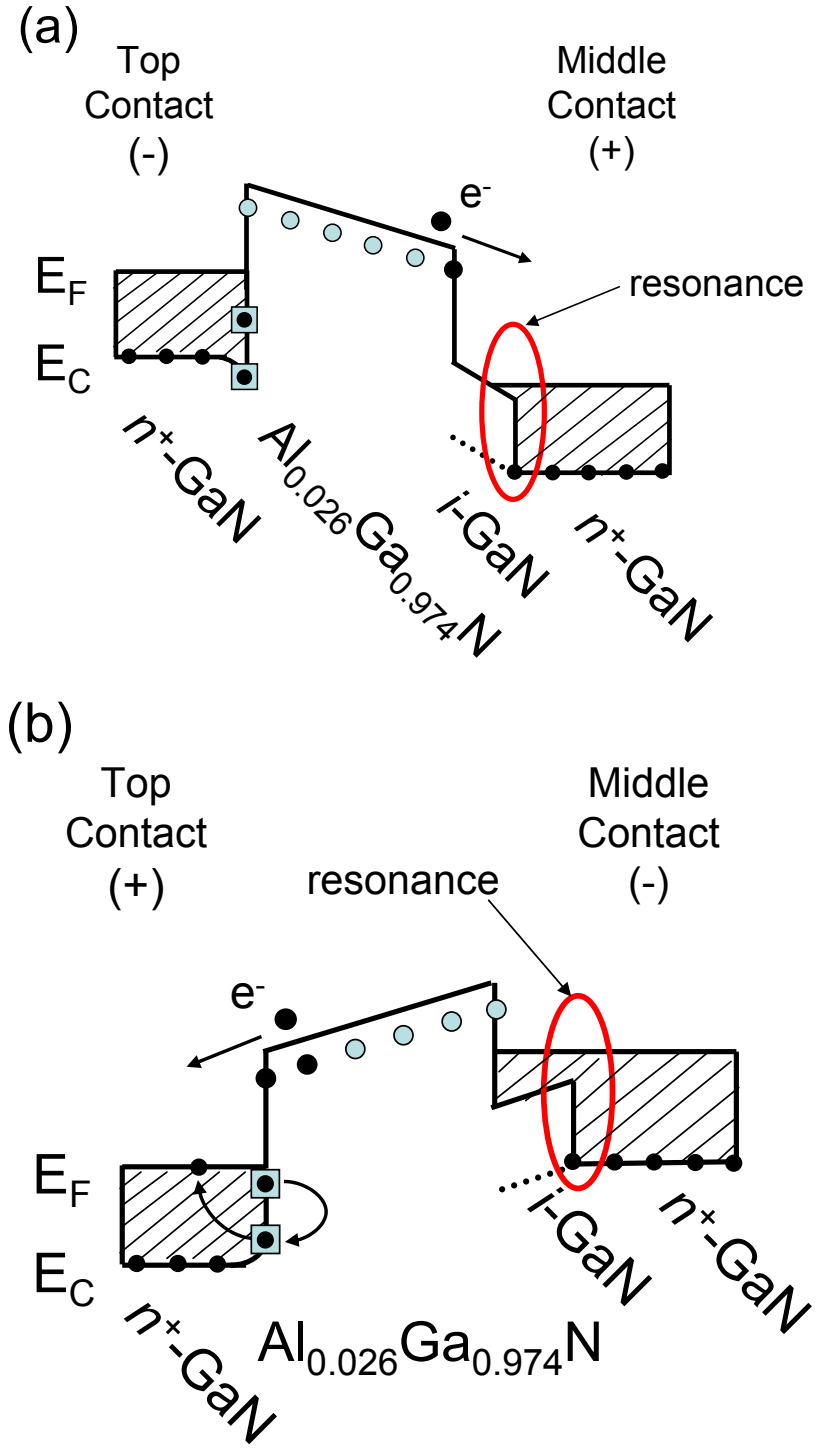

Figure 3.12: Band diagram of the 1291 structure under (a) reverse bias, and (b) forward bias. Resonance scattering can occur due to hybridization of the bound state levels of the deep Si-donor impurities in the band gap with excited states in the conduction band, resulting in the high-frequency capacitance peak. Negative capacitance was observed under forward bias due to an impact ionization-like process occurring at the n^+-GaN/$Al_{0.026}Ga_{0.974}N$ interface. Only the TC-MC layer is shown as the MC-BC layer is identical

Chapter 4

Conclusion

In summary, multiple defect states in 2- and 3-contact n^+-GaN/$Al_xGa_{1-x}N$ heterojunction photodetector structures were characterized based on capacitance measurements. A step in the capacitance and hysteresis effect were observed in the C-V profiles of the 2-contact sample with an Al fraction of 0.1. The hysteresis was attributed to the accumulation of charge at the heterointerface, when C-donor and/or N-vacancy defect energy states (with activation energy of 149±1 meV) were present at the interface just above the Fermi level. The Al fraction in the barrier layer was found to strongly influence the capacitance characteristics of the samples, as the Al fraction in the barrier layer not only changed the work function at the interface but, more importantly, changed the position of the interface trap states relative to the Fermi level.

When the Al fraction was lowered to 0.026, C-V and C-f profiles of the the 2-contact samples showed negative capacitance and FDCD. Using both IR spectroscopy and thermal activation energies, the fast traps states ($\tau_2 = 1.77 \pm 0.05$ μs) are attributed to C-donor/N-vacancy and deep Si-donor defect states located at the heterointerface with activation energies of approximately 125±1 and 140±2 meV, respectively; and the slow trap states ($\tau_1 = 155 \pm 9$ μs) are attributed to shallow Si-donor impurities located in the $Al_{0.026}Ga_{0.974}N$ barrier layer with an optical activation energy

of 30.8±0.2 meV and a thermal activation energy of 15±1 meV. Shallow Si-donor states in the $Al_{0.1}Ga_{0.9}N$ barrier of sample 1547 were also observed, with an activation energy of 30.9±0.1 meV. Although multiple methods of determining activation energies allows for the identification of impurity traps, the additional use of C-V and C-f measurements provide information about the effects these trap states have on the electronic and optical properties of n^+-GaN/$Al_xGa_{1-x}N$ detectors.

Results from the 2-contact n^+-GaN/$Al_xGa_{1-x}N$ structures provided a basic framework for expanding the capacitance analysis to the 3-contact n^+-GaN/$Al_xGa_{1-x}N$/i-GaN/n^+-GaN structures. The i-GaN buffer layer was included in the 3-contact structure to reduce the amount of Si migrating into the $Al_xGa_{1-x}N$ barrier. However, this buffer layer introduced additional interfaces into the system, further complicating the original situation. It was found that negative capacitance originated from C-donor/N-vacancy and deep Si-donor defect states at the n^+-GaN/$Al_{0.026}Ga_{0.974}N$ heterojunction, with activation energies of 125±1 and 139±2 meV, respectively. A high-frequency capacitance peak was observed in the C-f profiles, a result of resonance scattering due to hybridization of localized Si-donor defect states in the band gap (with electronic levels above the conduction band minimum) and continuous conduction band states at the i-GaN/n^+-GaN interface. The defect states active at the i-GaN/n^+-GaN interface had relaxation times between 1.61 and 2 μs, similar to the fast trap states observed in the 2-contact n^+-GaN/$Al_{0.026}Ga_{0.974}N$ structures. Table 4.1 summarizes the results from all UV/IR dual-band structures studied.

C-donor and N-vacancy related impurities are known to be incorporated into the material from the utilized organic precursors, [4] such as the TMGa, TMAl, or ammonia used as the Ga, Al, and N precursors, respectively, and defects in the crystalline structure. Si-donor related impurities are due to dopant migration from the top- (or bottom-) contact layers. The concentration of Si-donor traps have been found to correlate with the flow rate of SiH_4 during the growth process. [24]

Table 4.1: Summary of sample parameters, defect state related activation energies, and observed capacitance characteristics for all dual-band detectors studied.

	Sample Number			
	2-contact		3-contact	
	1547	1158	1291	1300
Al fraction	0.1±0.001	0.026±0.001	0.026±0.001	0.026±0.001
Free carrier response (μm)	3-8	8-13	8-13	8-13
Shallow Si-donor (meV)	30.9±0.1	30.8±0.2		
C-donor/N-vacancy (meV)	149±1	125±1	125±1	125±1
Deep Si-donor (meV)		140±2	139±2	136±2
Relaxation times (μs)	68-107	1.74±0.1	1.67-2	1.67-2
FDCD	yes	yes	yes	yes
Capacitance-step	yes	no	no	no
Capacitance Hysteresis	yes	no	no	no
Negative Capacitance	no	yes	yes	yes*
High-frequency capacitance peak	no	no	yes	yes

* Negative capacitance is only observed for TC-MC

Bibliography

[1] M. P. Touse, G. Karunasiri, K. R. Lantz, H. Li, and T. Mei, "Near- and mid-infrared detection using GaAs/$In_xGa_{1-x}As$/InGaAs multiple step quantum wells," Appl. Phys. Lett. **86**, 093501 (2005).

[2] J. Li, K. K. Choi, and D. C. Tsui, "Voltage-tunable four-color quantum-well infrared photodetectors," Appl. Phys. Lett. **86**, 211114 (2005).

[3] G. Ariyawansa et al., "Near-and far-infrared *p*-GaAs dual-band detector," Appl. Phys. Lett. **86**, 143510 (2005).

[4] G. Ariyawansa et al., "GaN/AlGaN ultraviolet/infrared dual-band detector," Appl. Phys. Lett. **89**, 091113 (2006).

[5] D. Starikov, C. Boney, R. Pillai, and A. Bensaoula, *Proceedings the ISA/IEEE Sensors for Industry Conference 2004*, New Orleans, LA, 2004 (IEEE, Piscataway, NJ, 2004), pp. 3640.

[6] E. Munoz, E. Monroy, J. L. Pau, F. Calle, F. Omnes, and P. Gibart, "III nitrides and UV detection," J. Phys.: Condens. Matter, **13**, 7115 (2001).

[7] G. Ariyawansa et al., "GaN/AlGaN heterojunction infrared detector responding in 8-14 and 20-70 μm ranges," Appl. Phys. Lett. **89**, 141122 (2006).

[8] R. M. Chu, Y. G. Zhou, K. J. Chen, and K. M. Lau, "Admittance characterization and analysis of trap states in AlGaN/GaN heterostructures," phys. stat. sol. (c) **0**, 2400 (2003).

[9] U. Ozgur, G. Webb-Wood, H. O. Everitt, F. Yun, and H. Morkoc, "Systematic measurement of $Al_xGa_{1-x}N$ refractive indiced," Appl. Phys. Lett. **79**, 4103 (2001).

[10] E. F. Schubert, *Doping in III-V Semiconductors*, (Cambridge: University Press, 1993).

[11] Y. N. Yang, D. D. Coon, and P. F. Shepard, "Thermionic emission in silicon at temperatures below 30 K," Appl. Phys. Lett. **45**, 752 (1984).

[12] R. N. Bhatt and T. M. Rice, "Single-particle energy levels in doped semiconductors at densities below the metal-nonmetal transition," Phys. Rev. B **23**, 1920 (1981).

[13] D. C. Look, D. C. Reynolds, J. W. Hemsky, J. R. Sizelove, R. L. Jones, and R. J. Molnar, "Defect Donor and Acceptor in GaN," Phys. Rev. Lett. **79**, 2273 (1997).

[14] T. Lindner, G. Paasch, and S. Scheinert, "Hysteresis in organic field-effect devices: Simulated effects due to trap recharging," J. Appl. Phys. **98**, 114505 (2005).

[15] A. G. U. Perera, W. Z. Shen, M. Ershov, H. C. Liu, M. Buchanan, and W. J. Schaff, "Negative Capacitance of GaAs Homojunction Far-Infrared Detectors," Appl. Phys. Lett. **74**, 3167 (1999).

[16] W. L. Liu, Y. L. Chen, A. A. Balandin, and K. L. Wang, "Capacitance-Voltage Spectroscopy of Trapping States in GaN/AlGaN Heterostructure Field-Effect Transistors," J. Nanoelectron. Optoelectron. **1**, 258 (2006).

[17] M. Ershov, H. C. Liu, L. Li, M. Buchanan, Z. R. Wasilewski, and A. Jonscher, "Negative Capacitance Effects in Semiconductor Devices," IEEE Trans. Electron Devices **45**, 2196 (1998).

[18] X. Wu, E. S. Yang, and H. L. Evans, "Negative capacitance at metal-semiconductor interfaces," J. Appl. Phys. **68**, 2845 (1990).

[19] M. Ershov, H. C. Liu, L. Li, M. Buchanan, Z. R. Wasilewski, and V. Ryzhii, "Unusual capacitance behavior of quantum well infrared photodetectors," Appl. Phys. Lett. **70**, 1828 (1997).

[20] W. J. Moore, J. A. Freitas, and R. J. Molnar, "Zeeman spectroscopy of shallow donors in GaN," Phys. Rev. B **56**, 12073 (1997).

[21] H. Wang and A. B. Chen, "Calculation of shallow donor levels in GaN," J. Appl. Phys. **87**, 7859 (2000).

[22] M. Sumiya, K. Yoshimura, K. Ohtsuka, and S. Fuke, "Dependence of impurity incorporation on the polar direction of GaN film growth," Appl. Phys. Lett. **76**, 2098 (2000).

[23] V. Bougrov, M. Levinshtein, S. Rumyantsev, and A. Zubrilov, *Properties of Advanced Semiconductor Materials*, (New York: Wiley, 2001).

[24] W. Gotz, N. M. Johnson, C. Chen, H. Liu, C. Kuo, and W. Imler, "Activation energies of Si donors in GaN," Appl. Phys. Lett. **68**, 3144 (1996).

[25] V. I. Okulov, "Effects of resonance scattering of electrons by donor impurities in semiconductors," Low Temp. Phys. **30**, 897 (2004).

[26] C. Skierbiszewski, T. Suski, M. Leszczynski, M. Shin, M. Skowronski, M. D. Bremser, and R. F. Davis, "Evidence for localized Si-donor state and its metastable properties in AlGaN," Appl. Phys. Lett. **74**, 3833 (1999).

[27] C. G. Van de Walle and J. Neugebauer, "First-principles calculations for defects and impurities: Applications to III-nitrides," Appl. Phys. Rev. **95**, 3851 (2004).

[28] A. I. Agafonov and E. A. Manykin, "Impurity-induced narrow bands of continuous electronic states in doped semiconductors," Phys. Rev. B **52**, 14 571 (1995).

[29] G. Govindaraj and R. Murugaraj, "A new anomalous relaxation function and electrical properties of disordered materials," Mater. Sci. Eng. **B77**, 60 (2000).

Appendix: Monte Carlo Simulations

1. Negative Capacitance

A Monte Carlo simulation was written in order to model negative capacitance in the C-f profiles of sample 1158. In this model, contributions from both majority and minority carriers are included. The following expression was used in the calculation, which assumes Debye relaxation:

$$C(\omega) = C_0 + \frac{a_1}{1 + (\omega\tau_1)^2} - \frac{a_2}{1 + (\omega\tau_2)^2}. \tag{A.1}$$

where C_0 is the geometric capacitance, a_1 and a_2 are constants, and τ_1 and τ_2 are the relaxation times of the majority and minority carriers, respectively. The program calculates values for the 5 variables that will minimize the difference between the randomly drawn values and the experimental data.

```
/*
    Monte Carlo Capacitance.cc
    Laura Byrum

    Monte Carlo simulation to model negative capacitance observed in the C-V-f profiles
    of sample 1158
*/

#include <iostream>
#include <math.h>
#include <fstream>
#include <stdio.h>

using namespace std;
int main()

{
    ofstream outputFile;
    outputFile.open("/Users/Lab/Desktop/Capacitance Simulation/Capacitance 2-contact.
txt");

    outputFile.setf(ios::scientific);
    outputFile.precision(6);

    cout.setf(ios::scientific);
    cout.precision(6);

    // Manually define data array of 23 elements for 1158-1H 0V

    float Ccalc;

    float w[23] = {1.00e6, 9.60e5, 8.00e5, 6.00e5, 5.00e5, 4.80e5, 4.00e5, 3.33e5,
                   3.00e5, 2.4e5, 2.00e5, 1.5e5, 1.00e5, 9.60e4, 8.00e4, 7.14e4,
                   6.00e4, 5.00e4, 4.00e4, 2.00e4, 1.00e4, 7.50e3, 6.00e3};

    float C[23] = {7.495670e-11, 7.760860e-11, 7.906060e-11, 9.449150e-12,
                   -8.959900e-11, -1.12162e-10, -1.884220e-10, -2.2351e-10,
                   -2.312910e-10, -2.353520e-10, -2.25271e-10, -2.333380e-10,
                   -2.113780e-10, -2.101760e-10, -2.039230e-10, -2.007980e-10,
                   -1.952850e-10, -1.891180e-10, -1.803550e-10,  -1.382440e-10,
                   -5.473700e-11, -1.334410e-11, 1.877540e-11 };



    float Co;
    float A1, A2, tau1, tau2;
    //geometric capacitance Co = epsilon*epsilono*(mesa area)/(barrier thickness)
    //Co = 2.922e-11;   from calculations with mesa parameters
```

```
float sum;
float Diff;

int j, i;

outputFile << "chai squared=    " << "Co =      " << "tau1 =        " << "tau2 =
" << "A1 =      " << "A2 =      " << endl;

outputFile << endl;
j = 0;
while (j < 10000)       // run 10,000 iterations
{
    sum = 0;


    float Comin, Comax;
    Comin = 5e-11;
    Comax = 2.2e-10;
    float dCo = Comax - Comin;

    Co =Comax - dCo*((float)rand())/RAND_MAX;

    float tau1min, tau1max;
    tau1min = 120e-6;
    tau1max = 180e-6;
    float dtau1 = tau1max - tau1min;

    tau1 = tau1max - dtau1*((float)rand())/RAND_MAX;

    float tau2min, tau2max;
    tau2min = 1.30e-6;
    tau2max = 1.85e-6;
    float dtau2 = tau2max - tau2min;

    tau2 = tau2max - dtau2*((float)rand())/RAND_MAX;


    float a1min, a1max;
    a1min = 4.5e-10;
    a1max = 5e-10;
    float da1 = a1max - a1min;

    A1 = a1max - da1*((float)rand())/RAND_MAX;


    float a2min, a2max;
    a2min = 4.5e-10;
```

```
        a2max = 5e-10;
        float da2 = a2max - a2min;

        A2 = a2max - da2*((float)rand())/RAND_MAX;



            for(i = 0; i <=  22; i ++)
                {
                Ccalc = Co + (A1)/(1 + pow(tau1*w[i],2)) - (A2)/(1 + pow(tau2*w[i],2));

                Diff = (Ccalc - C[i]);

                sum += Diff*Diff;
                                }

        // only output data if chi^2 value is less than user defined "sum

        if (sum < 3.15e-20)
        {
            outputFile << sum << "  " << Co << "    " << tau1 << "  " << tau2 << "  "
            << A1 << "  " << A2 << endl;

            j++;
            printf("%d\n", j);
        }

    }

    outputFile.close();


return 0;
}
```

2. High-frequency Capacitance Peak

A Monte Carlo simulation, similar to the one described above, was used to model the high-frequency capacitance peak in the 1291 samples. The peak could be modeled using the equation:

$$C(\omega) = C_0 + \frac{a_1}{1+\omega^2\tau_1^2} - \frac{a_2}{1-\omega^2(\tau_2{}' - \tau_2{}'')^2}. \tag{A.2}$$

where C_0 is the geometric capacitance, a_1 and a_2 are constants, and τ_1 is the relaxation times of the majority carriers. In this case, the minority carries have a complex relaxation time $\tau_2^\star = \tau_2{}' - i\tau_2{}''$ where $\tau_2{}'$ and $\tau_2{}''$ are the real and imaginary part of $\tau_2^\star$, respectively. The essential difference in this model as compared to the previous one, is the negative sign in the denominator of the last term (contribution from minority carriers). The negative sign will allow for a pole at $1 = \omega^2(\tau_2{}' - \tau_2{}'')^2$, which is observed as the high frequency capacitance peak. The program calculates values for the 5 variables that will minimize the difference between the randomly drawn values and the experimental data.

```
/*
   Monte Carlo Capacitance.cc
    Laura Byrum

    Monte Carlo simulation to model the high-frequency capacitance peak observed in the
    C-f profiles of sample 1291
*/

#include <iostream>
#include <math.h>
#include <fstream>
#include <stdio.h>

using namespace std;
int main()

{
    ofstream outputFile;
    outputFile.open("/Users/Lab/Desktop/Capacitance Simulation/Capacitance 3-contact.
txt");

    outputFile.setf(ios::scientific);
    outputFile.precision(6);

    cout.setf(ios::scientific);
    cout.precision(6);

    //Manually define data array of 20 elements for 1291-1D 0V

    float Ccalc;

    float w[20] = {1.00e6, 9.60e5, 8.00e5, 6.00e5, 5.00e5, 4.80e5, 4.00e5, 3.33e5,
                   3.00e5, 2.4e5, 2.00e5, 1.5e5, 1.00e5,9.60e4,8.00e4, 7.2428e4,
                   6.00e4, 5.00e4, 4.00e4, 3.00e4};

    float C[20] = {4.94287E-10, 4.99383E-10, 5.20573E-10, 4.99664E-10, 3.45459E-10,
                   3.15173E-10, 2.61289E-10, 2.66151E-10, 2.71764E-10, 2.83325E-10,
                   2.8967E-10, 2.95901E-10, 3.00356E-10, 3.00796E-10, 3.01982E-10,
                   3.02601E-10, 3.03305E-10, 3.03999E-10, 3.04305E-10, 3.05072E-10};




    float Co;
    float a1, a2, tau1, tau2;

    float sum;
    float Diff;
```

```
int j, i;

outputFile << "chai squared=    " << "Co =      " << "tau1 =    " << "tau2 =    "
            << "a1 =        " << "a2 =      " << endl;

outputFile << endl;
j = 0;
while (j < 10000)       // run 10,000 iterations
{
    sum = 0;

    float Comin, Comax;
    Comin = 3.0e-10;
    Comax = 3.3e-10;
    float dCo = Comax - Comin;

    Co =Comax - dCo*((float)rand())/RAND_MAX;


    float tau1min, tau1max;
    tau1min = 140e-6;
    tau1max = 175e-6;
    float dtau1 = tau1max - tau1min;

    tau1 = tau1max - dtau1*((float)rand())/RAND_MAX;


    float tau2min, tau2max;
    tau2min = 1.25e-6;
    tau2max = 1.80e-6;
    float dtau2 = tau2max - tau2min;

    tau2 = tau2max - dtau2*((float)rand())/RAND_MAX;


    float a1min, a1max;
    a1min = 1e-14;
    a1max = 7e-14;
    float da1 = a1max - a1min;

    a1 = a1max - da1*((float)rand())/RAND_MAX;


    float a2min, a2max;
    a2min = 1e-11;
    a2max = 2e-11;
    float da2 = a2max - a2min;

    a2 = a2max - da2*((float)rand())/RAND_MAX;
```

```
            for(i = 0; i <=  19; i ++)
                {
                Ccalc = Co + (a1)/(1 + pow(tau1*w[i],2)) - (a2)/(1 - pow(tau2*w[i],2));

                Diff = (Ccalc - C[i]);

                sum += Diff*Diff;
                                }

        // only output data if chi^2 value is less than user defined "sum

        if (sum < 9.5e-20)
        {
            outputFile << sum << "  " << Co << "    " << tau1 << "  " << tau2 << "  "
            << a1 << "  " << a2 << endl;

            j++;
            printf("%d\n", j);
        }

    }

    outputFile.close();


return 0;
}
```